



## RESEARCH ARTICLE

10.1029/2024MS004330

## Key Points:

- We present a method for estimating ocean anthropogenic carbon based on marine carbonate system data and a water mass mixing framework
- Key advantages of our method include reliance on climatologies derived from accurate observations and accounting for oxygen disequilibrium
- We determined a global ocean anthropogenic carbon inventory of  $124 \pm 7$  Pg C referred to 1995, consistent with estimates from other methods

## Supporting Information:

Supporting Information may be found in the online version of this article.

## Correspondence to:

M. López-Mozos,  
mlopezm@iim.csic.es

## Citation:

López-Mozos, M., Pérez, F. F., Carracedo, L. I., Gebbie, G., & Velo, A. (2025). A novel back-calculation approach to estimate ocean anthropogenic carbon using carbon-based data and a total matrix intercomparison method. *Journal of Advances in Modeling Earth Systems*, 17, e2024MS004330. <https://doi.org/10.1029/2024MS004330>

Received 6 MAR 2024

Accepted 3 DEC 2024

## Author Contributions:

**Conceptualization:** M. López-Mozos, F. F. Pérez, A. Velo

**Data curation:** M. López-Mozos, G. Gebbie, A. Velo






**Formal analysis:** M. López-Mozos, F. F. Pérez, L. I. Carracedo, A. Velo

**Funding acquisition:** F. F. Pérez, A. Velo

**Investigation:** M. López-Mozos, F. F. Pérez, L. I. Carracedo

© 2025 The Author(s). Journal of Advances in Modeling Earth Systems published by Wiley Periodicals LLC on behalf of American Geophysical Union. This is an open access article under the terms of the [Creative Commons Attribution-NonCommercial-NoDerivs License](#), which permits use and distribution in any medium, provided the original work is properly cited, the use is non-commercial and no modifications or adaptations are made.

# A Novel Back-Calculation Approach to Estimate Ocean Anthropogenic Carbon Using Carbon-Based Data and a Total Matrix Intercomparison Method

M. López-Mozos<sup>1,2</sup> , F. F. Pérez<sup>1</sup> , L. I. Carracedo<sup>3</sup> , G. Gebbie<sup>4</sup> , and A. Velo<sup>1</sup> 

<sup>1</sup>Instituto de Investigaciones Marinas (IIM-CSIC), Vigo, Spain, <sup>2</sup>Facultad de Ciencias del Mar, Universidade de Vigo, Vigo, Spain, <sup>3</sup>University Brest, CNRS, Ifremer, IRD, Laboratoire d'Océanographie Physique et Spatiale (LOPS), IUEM, Plouzané, France, <sup>4</sup>Department of Physical Oceanography, Woods Hole Oceanographic Institution, Woods Hole, MA, USA

**Abstract** Over the last decades, back-calculation (BC) techniques for ocean anthropogenic carbon ( $C_{\text{ant}}$ ) estimation have improved and evolved into different methodologies that are not exempt from various assumptions and limitations. No single optimal BC method exists to date for computing  $C_{\text{ant}}$ ; therefore, it is necessary to continue advancing the broad range of approaches. Here, we present a novel method based on the BC fundamentals that combines marine-carbonate-system (MCS) data and the Total Matrix Intercomparison (TMI) framework. This MCS-TMI approach differs from other BC methods by using the TMI to reconstruct deep-ocean biogeochemical properties and their preformed conditions. It also incorporates a global sea-air oxygen disequilibrium term, and a dynamic stoichiometric carbon-to-oxygen ratio that depends on the water-mass ideal time. The MCS-TMI yields a total  $C_{\text{ant}}$  inventory of  $124 \pm 7$  Pg C (referred to 1995), in good agreement with previous global  $C_{\text{ant}}$  climatologies. The MCS-TMI method uncertainty ( $\pm 5.6 \mu\text{mol kg}^{-1}$ ) is controlled by input-data errors that, nonetheless, have a minimal impact on the total  $C_{\text{ant}}$  inventory. In contrast, our total  $C_{\text{ant}}$  inventory uncertainty is governed by methodological errors, specifically those related to the TMI's boundary conditions. Our study demonstrates the effectiveness of MCS data-based climatologies in reconstructing a 3D gridded  $C_{\text{ant}}$  climatology, and the validity of ocean circulation transport operators for obtaining BC preformed conditions.

**Plain Language Summary** Since the industrial revolution, human-induced excess carbon dioxide ( $C_{\text{ant}}$ ) has been disrupting the carbon cycle. The ocean absorbs part of it, reducing atmospheric excess but causing severe consequences for marine systems. Oceanic  $C_{\text{ant}}$  storage is uneven, and estimates rely on indirect methods due to the impossibility of an analytical procedure for discerning the signal. To date, there is no optimal method for calculating  $C_{\text{ant}}$ . Progress is essential, and advancements are needed across various approaches. Back-calculation methods differ from the rest by using marine-carbonate-system (MCS) data, and their results serve as observational references. In this study, we present a novel approach for estimating marine  $C_{\text{ant}}$  globally, which relies on an improved back-calculation formulation and is based exclusively on climatological MCS high-quality data. Our resulting  $C_{\text{ant}}$  climatology agrees with previous global studies, underscoring the feasibility of our approach and emphasizing the relevance of accurate MCS data for climate change related research.

## 1. Introduction

The ocean plays a key role in climate regulation, storing 40 times more carbon than the atmosphere (Friedlingstein et al., 2023). Since the industrial revolution, the carbon cycle has been altered by the excess of atmospheric carbon dioxide ( $\text{CO}_2$ ) emissions from human activities ( $C_{\text{ant}}$ ), leading the ocean to counteract such  $\text{CO}_2$  increase by absorbing nearly a third of it (Gruber et al., 2019). The anthropogenic carbon ( $C_{\text{ant}}$ ) invasion into the ocean is increasing ocean acidity and causing severe impacts on marine systems (Bednaršek et al., 2023; Feely et al., 2023; IGBP, IOC, SCOR, 2013). Therefore, it is crucial to understand and quantify the oceanic  $\text{CO}_2$  uptake, storage, and distribution, particularly the anthropogenic component (Intergovernmental Panel on Climate Change IPCC, 2019). Nevertheless, both components of  $\text{CO}_2$ , that is, anthropogenic and natural, have high variability and uncertainties that are difficult to observe and quantify (Müller et al., 2023). This is particularly true for the  $C_{\text{ant}}$  signal, as it represents only a small fraction of the dissolved inorganic carbon pool ( $C_T$ ). Moreover, the  $C_{\text{ant}}$  signal

**Methodology:** M. López-Mozos, F. F. Pérez, L. I. Carracedo, A. Velo  
**Project administration:** F. F. Pérez, A. Velo  
**Resources:** M. López-Mozos, F. F. Pérez, A. Velo  
**Software:** M. López-Mozos, G. Gebbie, A. Velo  
**Supervision:** F. F. Pérez, L. I. Carracedo, A. Velo  
**Validation:** M. López-Mozos, F. F. Pérez  
**Visualization:** M. López-Mozos, F. F. Pérez  
**Writing – original draft:** M. López-Mozos  
**Writing – review & editing:** M. López-Mozos, F. F. Pérez, L. I. Carracedo, G. Gebbie, A. Velo

is not directly distinguishable from the natural component (Brewer, 1978; Chen & Millero, 1979), which has led to the development of various techniques to derive it indirectly.

Significant progress has been made in ocean  $C_{\text{ant}}$  estimates over the last few decades, as evidenced by the within-uncertainty agreement between  $C_{\text{ant}}$  inventories derived from independent methods (Khatiwala et al., 2013). This highlights the importance of using multiple approaches, each with its own limitations and regional biases.  $C_{\text{ant}}$  methodologies can be categorized into (a) model-based and (b) observation-based approaches. The model-based category includes Global/Regional Ocean Biogeochemical Models (GOBMs/ROBMs) and data assimilation models (e.g., OCIMv2021, DeVries, 2022), which provide  $C_{\text{ant}}$  estimates and forecasts that are highly valuable for climate-related predictions and decisions. Observation-based approaches include methods that use transient tracers' data (e.g., Green Function methods) or marine-carbonate-system (MCS) data (i.e., back-calculation techniques or repeated observations to infer decadal changes, such as the eMLR\* of Gruber et al., 2019; Müller et al., 2023). The synergy between model-based and observation-based approaches is fundamental. For instance, observational products are frequently used to assess GOBMs/ROBMs performance (e.g., DeVries et al., 2023; Fu et al., 2022), thereby emphasizing the importance of further advancement in observation-based  $C_{\text{ant}}$  estimates.

Marine data acquisition is advancing significantly by increasing the number, frequency and coverage of observations (e.g., <https://www.glodap.info/>), especially for MCS measurements. The quality standards implemented for MCS (e.g., <https://www.go-ship.org/DatReq.html>) are leading to the highest levels of accuracy in MCS data to date (Dickson et al., 2003). In addition, progress in BGC-Argo sensors (Johnson et al., 2017) supports the ongoing improvement of MCS data collection in the future. Therefore, the use of MCS data for  $C_{\text{ant}}$  estimation is becoming increasingly important, particularly given the limited lifespan of transient tracers, such as Chlorofluorocarbons (CFCs), and their uncertain long-term traceability.

Assessing  $C_{\text{ant}}$ -change rates (i.e., relative changes in  $C_{\text{ant}}$  storage) is fundamental (e.g., Müller et al., 2023) to fully understand how the ocean is storing the  $\text{CO}_2$  excess since pre-industrial times. However, to quantify the storage in terms of absolute total  $C_{\text{ant}}$  inventories, year-referenced  $C_{\text{ant}}$  estimates are necessary (e.g., Sabine et al., 2004). This, combined with the growing efforts by the scientific community to improve the acquisition, quality and availability of MCS data, fosters the advancement of back-calculation techniques, which were previously limited by the lack of high-quality MCS data (Bockmon & Dickson, 2015).

The back-calculation techniques (Brewer, 1978; Chen & Millero, 1979) were the first  $C_{\text{ant}}$  methods proposed. They attempt to deduce the anthropogenic fraction from the total  $C_T$  pool, basing this partition on  $\text{CO}_2$  observations. To do so, the biological activity is first subtracted from the  $C_T$  measurements, often inferred through changes in oxygen ( $\text{O}_2$ ) and total alkalinity ( $A_T$ ), to obtain its preformed condition, that is, the state at the time of last ventilation before biological activity had an impact. Subsequently, from the resulting preformed  $C_T$ , a pre-industrial reference value of preformed  $C_T$  is subtracted. Over time, back-calculation techniques have evolved, differing in their approaches while undergoing improvements that have resulted in methods for  $C_{\text{ant}}$  estimation at global ( $\Delta C^*$  method, Gruber et al., 1996; TrOCA method, Touratier & Goyet, 2004a, 2004b; Touratier et al., 2007) and regional ( $C_{\text{IPSL}}^\circ$ , Lo Monaco et al., 2005;  $\phi\text{Ct}^\circ$  method, Pardo et al., 2011; Vázquez-Rodríguez et al., 2009), scales. All of these methods have been extensively applied and validated (e.g., Pardo et al., 2014; Sabine et al., 1999, 2002, 2004; Vázquez-Rodríguez et al., 2012; see Khatiwala et al. (2013) for an extended review). However, some of their common assumptions are, to a certain extent, restrictive and could be addressed more realistically, such as  $\text{O}_2$  saturation ( $\Delta C^*$ , TrOCA,  $\phi\text{Ct}^\circ$ ), the use of linear methods for mixing modeling based on conservative variables (as in  $\Delta C^*$  or  $\phi\text{Ct}^\circ$ ), the exclusion of denitrification (TrOCA), the computation of pre-industrial tracers through parametrizations (e.g.,  $A_T$ , sea-air  $\text{CO}_2$  disequilibrium, TrOCA), or the use of a fixed oxygen-to-carbon stoichiometric ratio ( $r_{\text{o:c}}$ ).

The effect of organic matter (OM) remineralization on carbon is often estimated by a fixed ratio from oxygen consumption.  $r_{\text{o:c}}$  is actually subject to differ from that expected from the Redfield composition (Redfield et al., 1963) depending on the nature of the OM, that is, in the percentage of proteins, lipids and carbohydrates (Anderson, 1995; Anderson & Sarmiento, 1994; Fraga et al., 1998; Körtzinger et al., 2001). In fact, below depths of 1,000 m, where the flow of particulate material decreases, dissolved organic material (DOM) becomes more prevalent (e.g., Middelburg, 2019), coinciding with the presence of older water masses. DOM has different compositions and lifetimes (Hansell, 2013; Hansell & Carlson, 2014) and its reactivity has been demonstrated to

decrease along the deep branch of conveyor circulation (Sulpis et al., 2023), so the  $r_{o,c}$  could change depending on the age of the water masses. Additionally, back-calculation methods assume that during the formation of water masses they are in perfect equilibrium with the atmosphere, thus neglecting the sea-air oxygen disequilibrium that is frequently observed at the time of water mass formation and subduction (Duteil et al., 2013; Ito et al., 2004). This omission can lead to overestimations of oxygen consumption by up to 25% when calculated from Apparent Oxygen Utilization (AOU; Duteil et al., 2013). However, including the sea-air oxygen imbalance can be challenging because of the difficulty in obtaining the preformed oxygen content (Ito et al., 2004).

The behavior of the preformed variables matches that of the conservative tracers, and therefore they are not significantly altered as they circulate in the ocean, allowing for the tracking of the steady-state ocean circulation (Broecker, 1974). For variables that are subject to biological activity, and thus deviate from conservative behavior, back-calculation techniques have adopted different parameterizations as for the conservative tracers, even though they can exhibit non-conservative behavior in some regions (Matsumoto & Gruber, 2005). Additionally, preformed variables have also been estimated from surface parametrizations and later reconstructed in the deep ocean through an Optimum Multiparameter analysis (OMP; Tomczak & Large, 1989). However, the OMP mixing framework may neglect water masses with potential significance in the overall deep-ocean property distribution, which data-assimilated inversion models represent more accurately (Gebbie & Huybers, 2010). With higher resolution, and lower computational demand, such tools provide transport operators of a steady-state ocean circulation that have proven to be versatile for numerous applications, such as the modeling of preformed variables (Carter et al., 2021; Lauvset et al., 2020; Liang et al., 2023).

Here, we present a new approach for estimating the steady-state component of  $C_{ant}$  globally (see Text S1 in Supporting Information S1) that relies on a back-calculation formulation and input climatological data that are based on high-quality MCS data. Our approach includes: 1) a novel,  $2^\circ \times 2^\circ$  grid resolution, water mass mixing framework (TMI: Total Matrix Intercomparison; Gebbie & Huybers, 2010), which 2) avoids the use of linear regressions to estimate preformed variables, 3) allow us to pioneering account for global oxygen disequilibrium, and 4) to propose a dynamic stoichiometric, carbon to oxygen, ratio depending on the ideal time of the water mass. This synthesis paper is structured as follows. Section 2 provides details of the data used, the back-calculation formulation followed, the procedure for deep-reconstruction of variables, the estimation of their preformed conditions with the TMI, and the uncertainties associated. Section 3 presents the results and their discussion by: 3.1 showing the biogeochemical processes and other back-calculation formulation terms representation, 3.2 the resulting  $C_{ant}$  distribution and total inventory, including a validation through comparison with other methodologies, 3.3 sensitivity analysis, and 3.4  $C_{ant}$  distribution at depth to assess and validate  $C_{ant}$  results. Section 4 summarizes the main conclusions of the study and provides insights on remaining challenges and future work.

## 2. Materials and Methods

### 2.1. Back-Calculation Approach

Proposed by Brewer (1978) and Chen and Millero (1979), back-calculation techniques aim to separate the anthropogenic component from the total inorganic carbon pool by representing  $C_{ant}$  as the difference between the preformed total inorganic carbon content ( $C_T^\circ$ ) and the analogous in pre-industrial conditions ( $C_T^{\circ\pi}$ ) (Equation 1). Note that preformed conditions (denoted as  $^\circ$  hereafter) are the water parcel properties at the time of last ventilation, deduced by correcting non-physical effects experienced since the parcel left the (sub)surface (Equation 2).

$$C_{ant} = C_T^\circ - C_T^{\circ\pi} \quad (1)$$

$$C_T^\circ = C_T - \text{biogeochemical (bgc) effect} \quad (2)$$

In a back-calculation approach, the removal of the biogeochemical effect to obtain the preformed total inorganic carbon is based on the representation of the remineralization and the carbonate pump through changes in oxygen ( $\Delta O_2$ ) and total alkalinity ( $\Delta A_T$ ), respectively. Constant stoichiometric ratios are assumed, despite relationships that sometimes deviate from a fixed pattern of behavior (Anderson, 1995; Fraga et al., 1998; Körtzinger et al., 2001). For  $A_T$  changes ( $\Delta A_T = A_T - A_T^\circ$ ), no preformed alkalinity change over time is considered, this assumption being reasonably acceptable (Feely et al., 2004; Matsumoto & Gruber, 2005). However, how to

compute its preformed condition is subject to more debate. So far, all back-calculation methods assume that during water masses formation they are in perfect oxygen equilibrium with the atmosphere. Oxygen changes are often derived from Apparent Oxygen Utilization ( $\Delta O_2 = AOU = O_{2,sat} - O_{2,measured}$ ) assuming that AOU is equal to zero at surface, neglecting significant oxygen disequilibrium regions (Duteil et al., 2013; Ito et al., 2004).

The recognized  $\Delta C^*$  method (Gruber et al., 1996) does contemplate the pre-industrial  $CO_2$  drift compared to saturation at the time of water mass formation and subduction when obtaining the preformed condition of the pre-industrial  $C_T$ . This step introduced the pre-industrial sea-air  $CO_2$  disequilibrium term ( $\Delta C_{dis}^\pi$ ) in the  $C_T^{\circ\pi}$  calculation (Equation 3; Equation 4), expressed as the difference between the ocean-atmosphere partial pressure of  $CO_2$ , converted to carbon concentrations.

$$C_T^{\circ\pi} = C_T^{\pi SAT} + \Delta C_{dis}^\pi \quad (3)$$

Based on the original back-calculation framework by Brewer (1978) and Chen and Millero (1979) (Equation 1), including the preindustrial sea-air  $CO_2$  disequilibrium term proposed by Gruber et al. (1996) (Equation 3) leads to the expression:

$$C_{ant} = C_T - bgc \text{ effect} - C_T^{\pi SAT} - \Delta C_{dis}^\pi \quad (4a)$$

where  $C_T$  is the total inorganic carbon content of a sample; *bgc effect* is the biogeochemical effect;  $C_T^{\pi SAT}$  is the pre-industrial  $C_T$  in saturation; and  $\Delta C_{dis}^\pi$  is the pre-industrial sea-air  $CO_2$  disequilibrium. Replacing the biogeochemical effect:

$$C_{ant} = C_T - \frac{1}{r_{oc}} \cdot AOU - \frac{1}{2} \cdot \left[ A_T - A_T^\circ + AOU \cdot \left( \frac{1}{r_{on}} + \frac{1}{r_{op}} \right) \right] - C_T^{\pi SAT} - \Delta C_{dis}^\pi \quad (4b)$$

where  $A_T$  is the Total Alkalinity;  $A_T^\circ$  is the preformed Total Alkalinity; and  $r_{oc}$ ,  $r_{on}$  and  $r_{op}$  are the oxygen to carbon, oxygen to nitrogen and oxygen to phosphorus stoichiometric ratios. According to Gruber et al. (1996), this leads to:

$$C_{ant} = \Delta C^* - \Delta C_{dis}^\pi \quad (4c)$$

where  $\Delta C^*$  includes the first three terms of (Equation 4a).

As a novelty in this study, we considered a (i) preformed AOU term to capture the oxygen disequilibrium, and a (ii) denitrification correction, as proposed by Gruber and Sarmiento (1997), but following Carter et al. (2021):

$$C_{ant} = C_T - \frac{1}{r_{oc}} \cdot (AOU - AOU^\circ) + r_{c:n} \cdot \Delta N^* - \frac{1}{2} \cdot \left[ A_T - A_T^\circ + (AOU - AOU^\circ) \cdot \left( \frac{1}{r_{on}} + \frac{1}{r_{op}} \right) \right] - C_T^{\pi SAT} - \Delta C_{dis}^\pi \quad (5)$$

Remineralization
Carbonate pump

Preformed  $C_T$

where  $AOU^\circ$  is the preformed Apparent Oxygen Utilization (see Section 2.3);  $r_{c:n}$  is the carbon to nitrogen denitrification ratio; and  $\Delta N^*$  is equal to  $=(NO_3^- - NO_3^{\circ}) - 16(PO_4^{3-} - PO_4^{3-\circ})$ , where  $NO_3^-$  and  $PO_4^{3-}$  are the preformed nitrate and phosphate (see Section 2.3), respectively.

## 2.2. Data

We used the observation-based gridded products from Broullón et al. (2019, 2020), which provide global 3D monthly climatologies of Total Alkalinity ( $A_T$ ) and total inorganic carbon ( $C_T$ ) at  $1^\circ \times 1^\circ$  resolution. Both

products are centered in 1995 and encompass 102 surface-to-bottom vertical levels.  $A_T$  and  $C_T$  are the outputs from neural networks (NN) trained with data from Global Ocean Data Analysis Project version 2.2016 (GLO-DAPv2, 2016; Olsen et al., 2016) and applied to World Ocean Atlas 2013 V2 (WOA13 V2, here on WOA13; Locarnini et al., 2013; Zweng et al., 2013) monthly climatologies of temperature ( $T$ ), salinity ( $S$ ) and dissolved oxygen ( $O_2$ ). Nutrient fields were derived by applying CANYON-B NN (Bittig et al., 2018) to WOA13  $T$ ,  $S$  and  $O_2$  as input data, getting nitrate ( $\text{NO}_3^-$ ), phosphate ( $\text{PO}_4^{3-}$ ) and silicate ( $\text{SiO}_4^{4-}$ ). In our study, we used these same  $T$ ,  $S$ ,  $O_2$  and nutrients fields. Monthly climatological data were averaged to obtain a unique annual climatological value and interpolated to a  $2^\circ \times 2^\circ$  and 33 vertical levels resolution grid to match the TMI grid (see Section 2.3), using the Data-Interpolating Variational Analysis (DIVA; Troupin et al., 2012). Potential temperature ( $\theta$ ) and Apparent Oxygen Utilization (AOU) were calculated with the *Gibbs Seawater (GSW) Oceanographic* MATLAB Toolbox, by McDougall and Barker (2011). The pre-industrial  $C_T$  in saturation ( $C_T^{\text{SAT}}$ ) was calculated with CO2SYS for MATLAB (Lewis & Wallace, 1998; Sharp et al., 2021; van Heuven et al., 2011) with a pre-industrial  $\text{CO}_2$  partial pressure ( $p\text{CO}_2^{\text{pi}}$ ) set to 280  $\mu\text{atm}$ , an input pressure of 0 dbar, and using  $\theta$  and preformed  $A_T$ ,  $\text{PO}_4^{3-}$ ,  $\text{SiO}_4^{4-}$  (see Section 2.3) along with the  $K_1$  and  $K_2$  from Sulpis et al. (2020), as they cover a wide range of low temperatures,  $K_{\text{SiO}_4}$  from Dickson (1990),  $K_F$  from Pérez and Fraga (1987) and  $T_B$  of Uppström (1974).

Stoichiometric carbon to nitrogen denitrification ratio ( $r_{\text{c:n}}$ ) was adopted from Gruber and Sarmiento (1997). Different relationships have been proposed for oxygen to carbon, oxygen to nitrogen and oxygen to phosphorus stoichiometric ratios (Anderson, 1995; Anderson & Sarmiento, 1994; Fraga et al., 1998). We used the ratios proposed by Anderson and Sarmiento (1994) for oxygen to nitrogen and phosphorus. For oxygen to carbon ratio, the ratio proposed by Anderson (1995) is a better fit for older water masses that present more resistant DOM (Hansell, 2013), so we tested both Anderson and Sarmiento's (1994) and Anderson's (1995) and finally used an average of the two weighted by the TMI ideal age, that is, the average time since a water parcel was last in contact with the surface, according to:

$$r_{\text{oc}}^T = r_{\text{oc}}(S\&A\ 1994) \cdot (1 + \alpha_{\text{oc}} \cdot T), \text{ where}$$

$$\alpha_{\text{oc}} = (r_{\text{oc}}(A\ 1995) - r_{\text{oc}}(S\&A\ 1994)) / (r_{\text{oc}}(S\&A\ 1994) \cdot 1000)$$

where  $r_{\text{oc}}^T$  is an age-based oxygen to carbon stoichiometric ratio;  $r_{\text{oc}}(S\&A\ 1994)$  is the ratio proposed by Anderson and Sarmiento (1994) of 117/170;  $r_{\text{oc}}(A\ 1995)$  is the ratio proposed by Anderson (1995) of 106/150; and  $T$  is the mean or ideal age in years, at grid level, provided by the TMI (Gebbie & Huybers, 2012). Note that we adopt 1000 years as the maximum average age.

### 2.3. TMI and Estimate of Preformed Variables

The preformed variables refer to the properties of a water mass parcel that remain unchanged from the time of its last ventilation. In the case of conservative properties, their off-(sub)surface value is equivalent to that of the last ventilation, together with the result of mixing processes acting on the tracer (Broullón et al., 2019; Vázquez-Rodríguez et al., 2012). In contrast, the observed value of non-conservative properties is equal to the sum of its value if it were conservative (mixing) along with the biogeochemical effect.

Rather than relying on preformed (sub)surface-properties parametrization, and their subsequent deep ocean reconstruction through a classical OMP (Gruber et al., 1996; Pardo et al., 2011; Vázquez-Rodríguez et al., 2009), we assumed that winter surface properties represent the preformed conditions. This assumption is based on the fact that subduction primarily occurs during the respective winters of each hemisphere (Qiu & Huang, 1995; Williams et al., 1995), and thus the conditions of these months influence the preformed state of the variables (Iselin, 1939; Stommel, 1979). Therefore, we can reconstruct deep-ocean conditions from winter surface properties by using the geometry of water masses pathways provided by an ocean transport model (Transport Matrix Intercomparison, TMI hereafter; Gebbie & Huybers, 2010; Gebbie et al., 2023). The TMI is a data-assimilation inverse model constrained almost entirely from observations, since it is based on the inversion of modern-day climatologies of temperature, salinity, phosphate, nitrate, oxygen, and oxygen-18/oxygen-16 isotope ratios and provides a steady-state circulation in a  $2^\circ$ -by- $2^\circ$  horizontal resolution with a vertical discretization of 33 levels. A wider description of the TMI and its applications can be found in Gebbie and Huybers (2010, 2011, 2012).

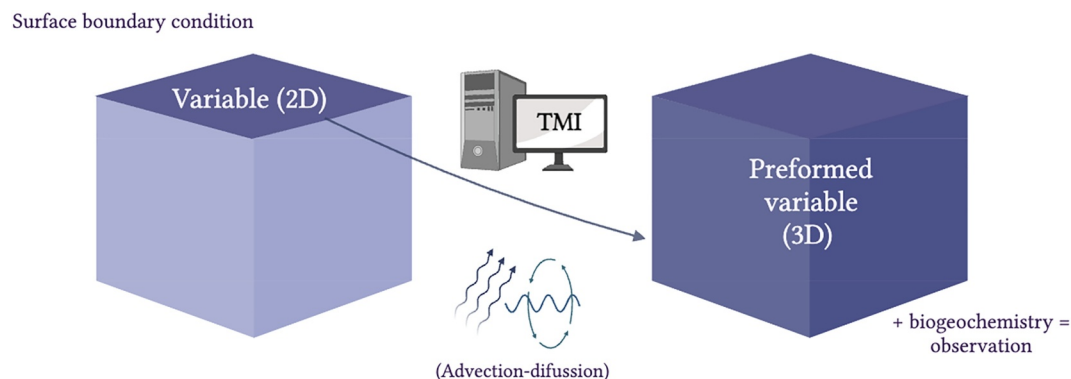


**Figure 1.** Simplified propagation scheme from a surface 2D variable to its 3D reconstruction at depth through the Total Matrix Intercomparison (TMI): imposing a surface boundary condition that best represents the surface preformed condition, this 2D layer propagates into the ocean interior through a steady-state inversion (no sink-sources considered). The 3D output provides a reconstruction of the ocean interior preformed property that is only affected by mixing, since the model does not account for non-physical effects. Thus, the difference between the observed property and the propagated one can be attributed to biogeochemistry; if it is a conservative tracer the difference must be equal to zero, if there are no residuals in the propagation.

We forced the surface boundary condition of the TMI with two types of data, that is, conservative and non-conservative tracers, and reconstruct their interior ocean distribution: for each ocean grid point the TMI provides the mixing fraction contribution that comes from the surface grid points. The three-dimensional (3D) field obtained only represents physical effects, as we excluded any sink-source processes in the deep ocean reconstruction. This results in preformed values for non-conservative properties or a deep reconstruction for conservative tracers. Then, we assume that differences between the observed properties and the analogous TMI-reconstructed properties (Figure 1), if any, can be attributed to biogeochemical processes.

Surface-boundary TMI input layers were estimated as the average of the monthly climatologies that best represent the water masses formation conditions according to latitude, that is: north of 20°N (south of 20°S) the average of January, February and March winter-months (July, August, September), and between 20°N and 20°S annual-average. The resulting winter-surface nitrate, phosphate and silicate layers were directly propagated, along with winter-AOU and  $\Delta C_{\text{dis}}^{\pi}$ , obtaining their preformed conditions ( $\text{NO}_3^-$ ,  $\text{PO}_4^{3-}$ ,  $\text{SiO}_4^{4-}$ ,  $\text{AOU}^{\circ}$ ) or deep reconstruction ( $\Delta C_{\text{dis}}^{\pi}$ ). Pre-industrial surface sea-air  $\text{CO}_2$  disequilibrium was estimated from Khatiwala et al. (2009) at surface by subtracting the product to the already computed  $C_T^{\circ}$  and  $C_T^{\pi\text{SAT}}$ , and then deep-reconstructing it with the TMI as a conservative tracer. The effect of the surface salinity was removed from the surface total alkalinity by a factor of 66.4 proposed by Carter et al. (2014), and the detached value was propagated into the ocean interior. The resulting field was undone by the same factor obtaining the preformed total alkalinity ( $A_T^{\circ}$ ).

#### 2.4. Results Validation

We used results from four independent  $C_{\text{ant}}$  methodologies (a back-calculation based method, two transient tracer data-based methods and a data-assimilated inversion model) to have a reference for our MCS-TMI estimates. In addition, we applied the TrOCA back-calculation method (Touratier et al., 2007) to evaluate the consistency of spatial patterns in our  $C_{\text{ant}}$  estimates. It is important to note that the TrOCA method has been shown to over-estimate global  $C_{\text{ant}}$  inventories by up to 50% (Yool et al., 2010). Therefore, we used TrOCA to validate our spatial distribution of  $C_{\text{ant}}$  rather than comparing absolute inventory values.

The first product used was Sabine et al. (2004), that provides a  $C_{\text{ant}}$  climatology centered in 1994, based on the back-calculation  $\Delta C^*$  method (Gruber et al., 1996), and whose formulation served as a basis for our approach. The  $\Delta C^*$  method assumes no sea-air oxygen disequilibrium but does include the  $\Delta C_{\text{dis}}^{\pi}$  with two ways to obtain the term, both assuming bulk advection and a single ventilation age. The second product used came from Lauvset et al. (2016), which follows a transit time distributions (TTD) approach. The methodology considers that the  $C_{\text{ant}}$  is a conservative tracer that can be reconstructed in the entire ocean through the ocean circulation transport represented by a - boundary propagator (Hall et al., 2002)—Green's function. Instead of using MCS data, the

TTD approach relies on transient tracers as CFCs to derive the statistical description of the age distribution. Lauvset et al. (2016) product provides a  $C_{\text{ant}}$  climatology centered in 2002 that we brought to 1995 for comparison to our results, according to

$$C_{\text{ant } 1995} = C_{\text{ant } 2002} \cdot [(1 + 0.0191)^{1995-2002}]$$

where  $C_{\text{ant } 1995}$  is the corrected  $C_{\text{ant}}$  for 1995 year;  $C_{\text{ant } 2002}$  is the original product; and 0.0191 is the annual increase rate determined by Gruber et al. (2019) between 1994 and 2007 for the global ocean.

In line with the TTD approach but refined, we also used the Khatiwala et al. (2009) product, which presents an evolution of the Green's function (GF) method. It considered twenty-six  $C_{\text{ant}}$  source regions and allowed the  $\Delta C_{\text{dis}}^{\pi}$  to undergo temporal and spatial changes for the first time. We used a 5-years  $C_{\text{ant}}$  average, centered at 1995. The product was regridded to the WOA13  $1^{\circ} \times 1^{\circ} \times 33$  levels grid by profile interpolation, and a constant density of  $1024.5 \text{ kg m}^{-3}$  was used for volumetric to mass conversion.

The last product we included was a data-assimilated inversion model that estimates  $C_{\text{ant}}$  distribution by considering it as a passive tracer within an abiotic carbon cycle model forced with atmospheric  $\text{CO}_2$  (DeVries, 2022), that would represent, in a way, an advance in the resolution of transient tracer data methods, both at the level of mixture scale and source regions.

Once all the products were homogenized (i.e., same resolution gridding and same reference year), the  $C_{\text{ant}}$  concentrations were vertically integrated to get the column inventories. Additionally,  $C_{\text{ant}}$  column inventories were horizontally integrated in five oceanic regions (North Atlantic, South Atlantic, North Pacific, South Pacific and Indian oceans), as well as in the sum of these, to quantitatively evaluate the differences of our results with respect to four other reference methodologies, following the regions evaluated in Müller et al. (2023) (Figure S1 in Supporting Information S1). Given the difference in spatial coverage and product grids, total  $C_{\text{ant}}$  (integrated at vertical and horizontal level, up to depth of 3.5 km) was normalized per product area and scaled to a reference area (see Table S1 in Supporting Information S2) to better compare among products. The TrOCA method was excluded in the total  $C_{\text{ant}}$  inventories comparison. Note that for  $\Delta C^*$  total  $C_{\text{ant}}$  inventories, negative values were set to zero according to literature (Müller et al., 2023; Sabine et al., 2004).

## 2.5. Sensitivity Analysis and Uncertainties

The MCS-TMI approach to estimate  $C_{\text{ant}}$  is subject to uncertainties that arise from two main sources: data-related errors and methodological errors. To evaluate the impact of each and quantify the overall uncertainty of our method, we conducted three sensitivity tests (*Case I, II* and *III*, described below) based on a Monte-Carlo analysis, with 300 simulations for each case.

In *Case I (data-related errors)* we quantified the uncertainty arising from errors in input data (WOA13 climatologies for  $T$ ,  $S$ ,  $\text{O}_2$ ) and their propagation to derived variables (NN-nutrients and  $A_T$  and  $C_T$ ). Since WOA13 climatologies do not provide error fields for the objectively analyzed  $T$ ,  $S$ ,  $\text{O}_2$  climatologies, we used the standard error of the mean (SE). We used surface SE values (with no spatial correlation for any of the variable pairs), and we computed the SE's standard deviation (STD) for each variable. To ensure a conservative final error estimate, we adopted a two-sigma criterion ( $p < 0.05$ ), resulting in introduced errors of  $0.32^{\circ}\text{C}$ ,  $0.12 \text{ PSU}$  and  $4\%$  for  $T$ ,  $S$  and  $\text{O}_2$ , respectively. We then generated 300 randomly perturbed fields for  $T$ ,  $S$ , and  $\text{O}_2$ , which served as inputs for the CANYON-B NN to estimate nutrients (resulting in 300 new 3D fields of  $\text{NO}_3^-$ ,  $\text{PO}_4^{3-}$ ,  $\text{SiO}_4^{4-}$ ). Ultimately, this ensemble data set (300 newly generated fields of  $T$ ,  $S$ ,  $\text{O}_2$ ,  $\text{NO}_3^-$ ,  $\text{PO}_4^{3-}$  and  $\text{SiO}_4^{4-}$ ) was used as input to NNGv2 (for  $A_T$ ) and NNGv2LDEO (for  $C_T$ ), generating 300 3D fields each of  $A_T$  and  $C_T$ . This procedure allowed errors in the derived variables (i.e., nutrients,  $A_T$  and  $C_T$ ) to more accurately reflect the data processing flowchart and any potential correlations or interactions among them. To isolate data-related errors, we kept the  $r_{\text{oc}}^T$  term and TMI surface boundary conditions constant in *Case I*, by only altering from the second vertical layer to the bottom and, therefore obtaining the same 3D-TMI reconstructed variables (preformed properties and  $\Delta C_{\text{dis}}^{\pi}$ ) for each simulation.

In *Case II (methodological errors)* we evaluated the uncertainty that results from variations in the  $r_{\text{oc}}^T$  term and the TMI surface boundary conditions. This analysis was divided into two sub-cases: *Case II - subtype I*, in which we assessed the sensitivity of the method to the  $r_{\text{oc}}^T$  term by setting a 10% of error in this parameter while keeping

the rest of variables unaltered; and *Case II - subtype 2*, in which we evaluated the uncertainty directly related to the TMI by introducing random errors only into the surface boundary conditions. For *Case II - subtype 2*, we used the 300 perturbed  $T$ ,  $S$  and  $O_2$  fields as in *Case I*, but only for the surface layer (while keeping the original data from the second vertical and below), and followed the subsequent processing workflow for nutrients and  $A_T$  and  $C_T$  as indicated for *Case I*. In addition, we considered a  $5 \mu\text{mol kg}^{-1}$  error for the surface  $\Delta C_{\text{dis}}^{\text{pr}}$  TMI input layer (Khaliwala et al., 2009 product).

Finally, *Case III (combined uncertainty)* represents the combined effect of both data-related and methodological errors (i.e., *Case I* and *Case II*), thereby serving as the reference case for estimating the total uncertainty in the MCS-TMI method. The total method uncertainty ( $\mu\text{mol kg}^{-1}$ ) was calculated as the mean of the STD 3D-matrix that resulted from the 300 Monte Carlo simulations in *Case III*. Additionally, the uncertainty of the total  $C_{\text{ant}}$  inventory (Pg C) was computed as the STD of the 300 total  $C_{\text{ant}}$  global inventories from *Case III*.

### 3. Results and Discussion

#### 3.1. Biochemical Processes Representation

The  $C_T^{\circ}$  in 1995 (Figure 2, panel H) results from the subtraction of the biological effect (Figure 2, panel B and C) to the  $C_T$ . Biogeochemical processes representation is one of the most important steps in a back-calculation approach. We represented them through changes in  $C_T$  due to the organic matter (OM) remineralization and the carbonate pump. Both the OM remineralization (Figure 2, panel B), and the excess of alkalinity due to  $\text{CaCO}_3$  dissolution (i.e., carbonate pump; Figure 2, panel C), presented a similar distribution, increasing their values from the North Atlantic as moving toward the North Pacific, after passing through the SO. Biogeochemical processes low-values in the North Atlantic coincide with the newly formed, and recently ventilated, North Atlantic Deep Water (NADW) water mass. The NADW is the most abundant water mass in the deep Atlantic (Liu & Tannya, 2021), and spreads southward mixing with the older Antarctic Bottom Water (AABW), that moves northwards in depth, along with the ventilated Antarctic Intermediate Water (AAIW), positioned above the NADW. Likewise, the AABW spreads toward the North Pacific and the Indian Ocean at depth, representing the dominant water mass at depth, with the AAIW also spreading northwards above the AABW. Consequently, both biogeochemical processes reach their maximum accumulation in the North Pacific, coinciding with the oldest water masses ages (Figure S2 in Supporting Information S1), and consistent with the well-described ocean circulation (Broecker & Peng, 1982; Talley, 2013). This evidences that, in terms of circulation patterns given by the TMI, biological processes are overall well reproduced in our approach, since they present an overall aging trend characterized by the extended time that water masses spend without contact with the atmosphere (Craig, 1971; Figure S2 in Supporting Information S1). Additionally, that the  $C_T^{\circ}$  has a consistent pattern when compared to its analog under pre-industrial conditions ( $C_T^{\text{pr}}$ ; Figure 2, panel I) also suggests a good integration and representation of the biological activity.

##### 3.1.1. Organic Matter Remineralization and $O_2$ Disequilibrium

The OM respiration (Figure 2, panel E), represented as the difference between the AOU and its preformed condition, controls most of the OM remineralization pattern and contributes up to 98.8% of its variability. Opposite, the denitrification pattern (Figure 2, panel K) has a low impact on OM remineralization when compared to respiration. The denitrification process contributes, in average, to the OM remineralization around  $0.8 \mu\text{mol kg}^{-1}$ , which is  $\sim 80$  times lower than the average contribution of respiration ( $64 \mu\text{mol kg}^{-1}$ ).

In general, respiration process is correlated with the water mass age. The more the time since the water mass left contact with the atmosphere the more biological aging (Craig, 1971; Figure S2 in Supporting Information S1), as the oxygen consumption due to respiration and then  $C_T$  release. This inverse pattern between the  $C_T$  and the respiration and their correlation with the water masses age is reflected in the age-based oxygen to carbon stoichiometric ratio proposed (Figure 2, panel D), that represents a function of the water masses ideal age according to respiration. Using the fixed  $r_{\text{o:c}}$  ratios from Anderson and Sarmiento (1994) and Anderson (1995) results in an average difference of  $\sim 5 \mu\text{mol kg}^{-1}$  of  $C_{\text{ant}}$  among them from ideal ages over 500 years (Figure S3 in Supporting Information S1), but particularly both generated an upward trend in the mean  $C_{\text{ant}}$  values as the water masses ideal age increases that the  $r_{\text{o:c}}^{\text{T}}$  proposed attenuates (Figure S3 in Supporting Information S1). Even so, in terms of OM respiration, shallow—recently formed—layers (up to  $\sim 500$  m) also present high oxygen utilization coinciding with high biological activity, wherein AOU may not be that elevated but increases rapidly. In particular, the



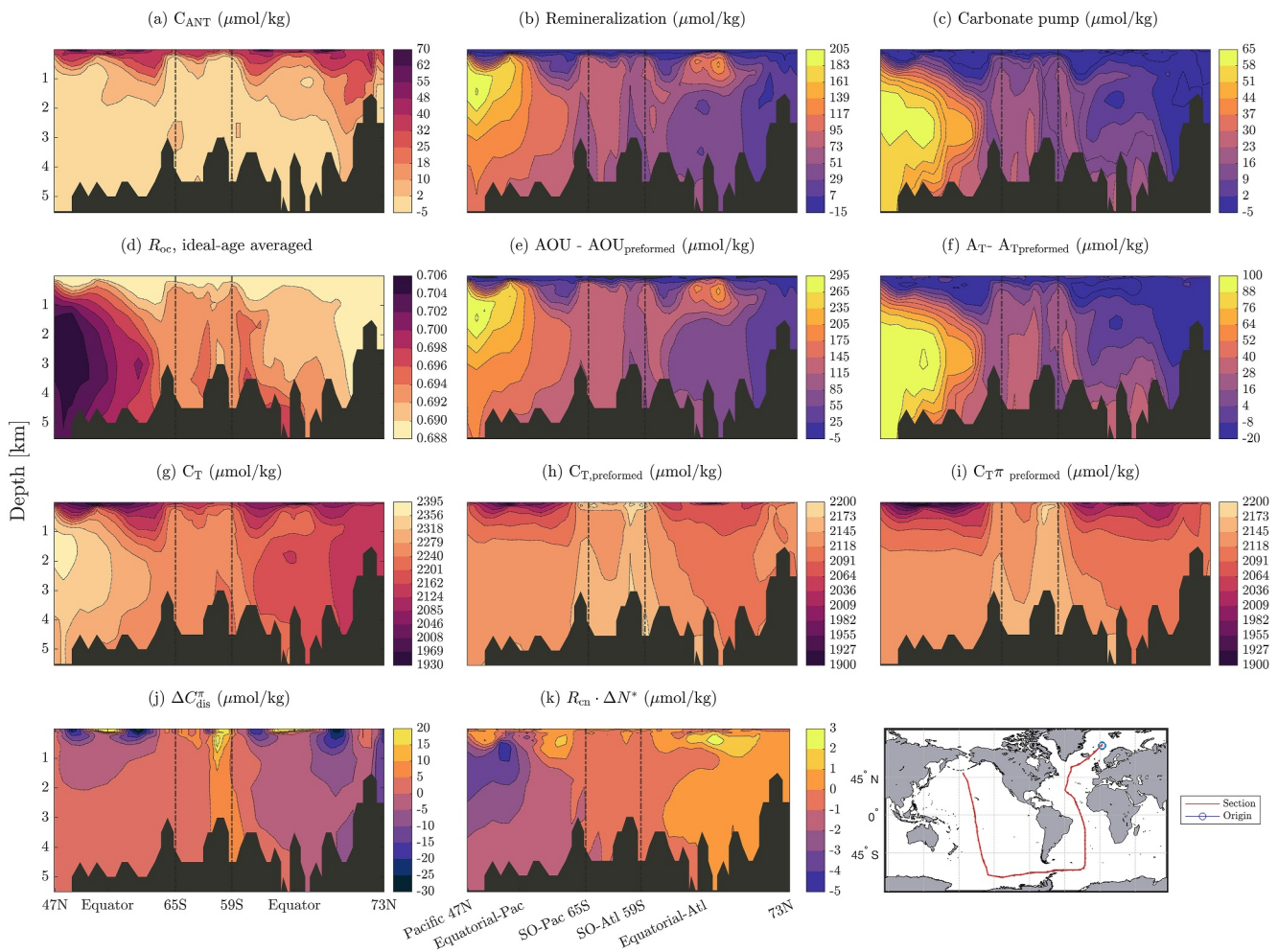


**Figure 2.** Transoceanic section, showing vertical  $C_{\text{ant}}$  distribution and biogeochemical and physicochemical processes (centered in 1995), from 73°N Atlantic up to 47°N Pacific, connecting the start-end section through the Southern Ocean (SO). The two vertical lines define the end of the Atlantic basin through the SO (SO-Atl 59°S), and the beginning of the Pacific basin (SO-Pac 65°S). Panels: (a) Anthropogenic carbon ( $C_{\text{ant}}$ ), (b) remineralization term (see Section 2.1), (c) carbonate pump term (see Section 2.1), converted to carbon concentrations, (d) age-based oxygen to carbon stoichiometric ratio, (e) difference between AOU and preformed AOU, (f) difference between Total Alkalinity and preformed Total Alkalinity, (g) total inorganic carbon from Broullón et al. (2020), (h) preformed total inorganic carbon, from subtracting biological panels B and C to panel G, (i) pre-industrial preformed total inorganic carbon, (j) sea-air  $\text{CO}_2$  disequilibrium and, (k) denitrification process, expressed in carbon concentrations.

Atlantic Ocean presents a shallow low-oxygen pool that coincides with the well-known Atlantic oxygen minimum zone, possibly generated because of a mixing limitation due to vertical and horizontal constraints, as boundaries formed by interactions with subtropical gyres, or warm temperatures (Carter et al., 2021).

As an improvement in a back-calculation approach, we considered a global sea-air  $\text{O}_2$  disequilibrium independent of the sea-air  $\text{CO}_2$  disequilibrium. Our approach uses the AOU, that reflects oxygen depletion relative to saturation, and the subtraction of its preformed condition ( $\text{AOU}^{\text{p}}$ ) corrects for the oxygen disequilibrium (Figure S4 in Supporting Information S1) that is often observed in deep water formation regions (Ito et al., 2004). Therefore, we inferred respiration from True Oxygen Utilization (TOU) instead of AOU (e.g., Ito et al., 2004; Koeve & Kähler, 2016). Until now, the only gaseous disequilibrium considered was the pre-industrial  $\text{CO}_2$  disequilibrium (Gruber et al., 2019; Sabine et al., 2004), which, when considered on its own, could erroneously include the  $\text{O}_2$  imbalance on it (Equation S1 in Supporting Information S1), and may underestimate the relevance of disequilibrium in carbon storage (Khawala et al., 2019). The correction increased the total  $C_{\text{ant}}$  inventory by 7.2 Pg C, indicating that not accounting for the  $\text{O}_2$  disequilibrium underestimates the total global  $C_{\text{ant}}$  inventory by 6%. When examining the respiration process, a bigger impact is observed, as it corrects the overestimation of oxygen consumption by up to 8.5%, when integrated globally. Thus, our results confirm the evidence that AOU-based

estimations overestimate respiration (Carter et al., 2021; Duteil et al., 2013), in particular in the South Atlantic and deep horizons, which agrees with Carter et al. (2021) that found the deep ocean and the Southern Ocean are the most impacted regions.

Furthermore, including the sea-air O<sub>2</sub> imbalance (i.e., using AOU-AOU<sup>o</sup>, or TOU, instead of AOU) in oxygen consumption reduces the unexplained variability of nitrate and phosphate depletion by 17% and 28% (Figure S5 in Supporting Information S1). Indeed, r<sub>o,n</sub> stoichiometric ratio (inferred from the inverse of the linear regressions slope), resulting from the adjustment after including sea-air O<sub>2</sub> imbalance in the AOU term (TOU), gets more centered between those of Anderson and Sarmiento (1994) for NO<sub>3</sub><sup>-</sup> and Anderson (1995) than the ones from assuming that O<sub>2</sub> is fully equilibrated in winter surface layer. Our results agree with a strong correlation between nutrients and oxygen consumption, presenting a similar correlation pattern with the ideal water masses age (Figure S2 and S5 in Supporting Information S1). This is also consistent with the most ΔN\* negative values, that is, higher denitrification, found in the Pacific Ocean (Figure 2) and Indian Ocean (Figure S6 in Supporting Information S1), as nitrate consumption increases when oxygen becomes limiting (Middelburg, 2019). However, the overall denitrification pattern does not exhibit a strong relationship with the ideal water masses age (R<sup>2</sup> = 0.41), or with TOU (R<sup>2</sup> = 0.55). The lack of correlation could be attributed to the presence of N<sub>2</sub> fixation zones or high TOU values in ventilated waters with high biological activity.

### 3.1.2. The Carbonate Pump

The carbonate pump (Figure 2, panel C) represents changes in A<sub>T</sub> due to formation and dissolution of calcium carbonate (CaCO<sub>3</sub>), along with the A<sub>T</sub> reduced by respiration-derived acids. The term is mostly mediated by the pattern of the difference between the A<sub>T</sub> and its preformed condition (Figure 2, panel F). However, the impact of the acid-derived biological effect (OM respiration) also affects, coinciding with previous studies that note its contribution throughout the water column (Liang et al., 2023). This is especially evident in the North Pacific, where respiration contributes to locate the accumulation carbonate pump maximum shallower than that of the total and preformed alkalinity difference by itself. This suggests that, when inferring the excess of alkalinity due to CaCO<sub>3</sub> dissolution, respiration representation is relevant, especially in old water masses. In turn, the deeper location of the carbonate pump maximum versus the remineralization maximum would be consistent since organic matter remineralization is potentially a faster, and shallower, occurring process (Carter et al., 2014, 2021; Francois et al., 2002; Klaas & Archer, 2002).

On the other hand, the carbonate pump presents a strong correlation with ideal water masses age (Figure S2 in Supporting Information S1), as well as the one that silicate opal dissolution (silicate increase) shows (Figure S5 in Supporting Information S1). In addition, there is a relationship between the carbonate pump and silicate consumption of 0.98 (Figure S5 in Supporting Information S1) close to the relationship of 0.96 shown by Rubin and Key (2002), which enforces the consistency of the TMI model when obtaining preformed nutrients.

### 3.2. Validation of the C<sub>ant</sub> Distribution at Global and Regional Scale

The C<sub>ant</sub> invasion in depth since the pre-industrial era is shown at Figure 2 at panel A, and shows an overall decrease in the C<sub>ant</sub> signal as depth increases. The largest C<sub>ant</sub> concentrations are found at the surface, where shallow and warm ocean layers are located, consistent with the fact that warmer waters present lower Revelle factor values (Broecker et al., 1979; Hauck & Völker, 2015; Zeebe & Wolf-Gladrow, 2001), meaning that are more efficient in the anthropogenic CO<sub>2</sub> uptake (Hauck & Völker, 2015; Sabine et al., 2004; Völker et al., 2002) than colder waters (Figure S7 in Supporting Information S1). In particular, the highest C<sub>ant</sub> concentrations are observed within subtropical regions, coinciding with Central Waters formation (Cianca et al., 2007; Talley, 2013; Álvarez et al., 2004). In these warm regions, the C<sub>ant</sub> signal penetrates in depth consistent with the described circulation of subtropical gyres (Reid, 1997), in contrast to equatorial upwelling regions where C<sub>ant</sub> vertical signal raises (Figure 2, panel A). Additionally, ocean circulation plays a key role in transporting C<sub>ant</sub>-rich waters from other regions to the subtropical gyres (DeVries et al., 2023), thereby enhancing the accumulation of C<sub>ant</sub> in these areas.

The depth-integrated spatial distribution of C<sub>ant</sub> (Figure 3, panel A) reveals the North Atlantic basin as the greatest C<sub>ant</sub> reservoir, with the Labrador Sea exhibiting the highest concentrations within the region. Thus, the deepest and strongest C<sub>ant</sub> vertical invasion is found in the North Atlantic (NA) basin (Figure 2, panel A), which coincides with previous studies (e.g., Gruber et al., 1996; Kötzinger et al., 1999; Wanninkhof et al., 1999), even extending

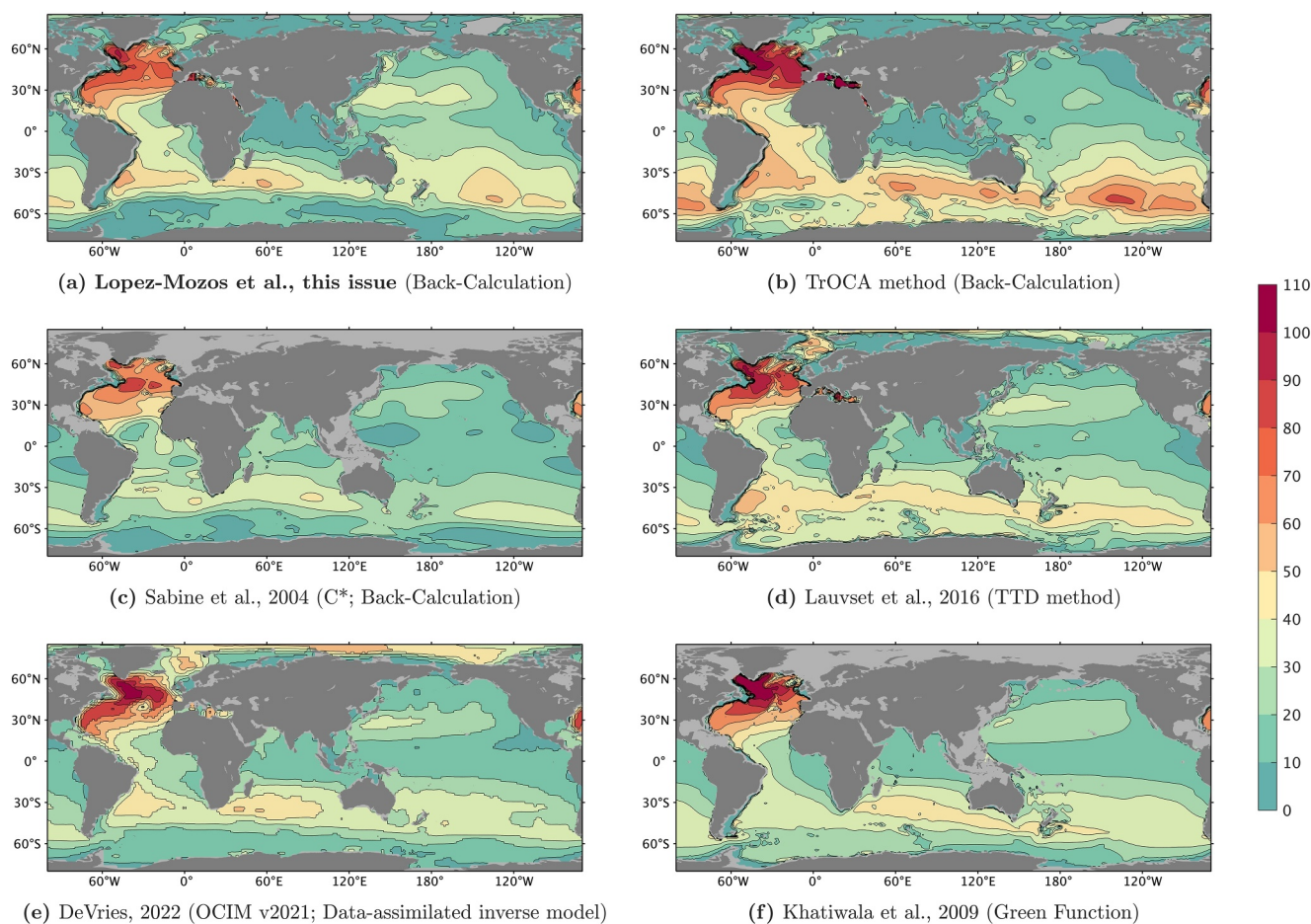


**Figure 3.**  $C_{\text{ant}}$  column inventories ( $\text{molC m}^{-2}$ ), centered in 1995, integrated from surface up to 3,500 m from six independent  $C_{\text{ant}}$  methodologies. Gray Arctic marine zones in panels (a) and (b) are negative out-of-scale values. For Sabine et al. (2004) product negative  $C_{\text{ant}}$  values have been maintained.

the  $C_{\text{ant}}$  signal below 3,000 m. Moreover, such invasion is consistent with the own basin circulation, where strong  $C_{\text{ant}}$  invasion is linked to the strong deep-ventilation (Fröb et al., 2018; Pérez et al., 2010). The  $C_{\text{ant}}$  pattern in the region shows a very similar distribution when compared to other methodologies (Figure 3), validating these results. Furthermore, when comparing total inventories quantitatively (Figure 4; see Section 2.4), our results (26.4 Pg C) are also consistent since they are inside the interquartile range for the NA, and in good agreement with the other four methods. In addition, the NA stands out as the largest  $C_{\text{ant}}$  reservoir per area globally (Table S1 in Supporting Information S2). However, our Nordic Seas  $C_{\text{ant}}$  column-inventory seems to be underestimated when compared to the TTD (Lauvset et al., 2016) and OCIMv21 (DeVries, 2022) approaches (Figure 3), which could also be supported by the fact that the region has been shown to be a present absorption area (Jeansson et al., 2023). This underestimation does not affect the NA total  $C_{\text{ant}}$  inventory, as the Nordic Seas is not included in the calculation of the NA total  $C_{\text{ant}}$  inventory. Not all products provide data for the Nordic Seas and Arctic region. Even so, a noticeable distinction is observed between our results and the TrOCA method (employed solely as an evaluative exercise of MCS data consistency) when compared to the GF and OCIMv2021. Both back-calculation approaches exhibit an almost identical lower pattern, suggesting a potential issue in the MCS data for the area. The fact that with the TrOCA exercise we utilize the same data aids in identifying possible flaws, indicating that divergences reflect genuine differences in approaches rather than arising from the use of different data sets. Conversely, convergences suggest consistency between the approaches.

There is a gradual decline in  $C_{\text{ant}}$  storage as we move southward into the South Atlantic (SA), culminating in a more significant accumulation within the SA subtropical gyre. Additionally, a zonal gradient is observed with elevated  $C_{\text{ant}}$  values along the western margin of the Atlantic. The described pattern coincides with the rest of methodologies (Figure 3), with which we also agree on the presence of a  $C_{\text{ant}}$  accumulation belt that connects the

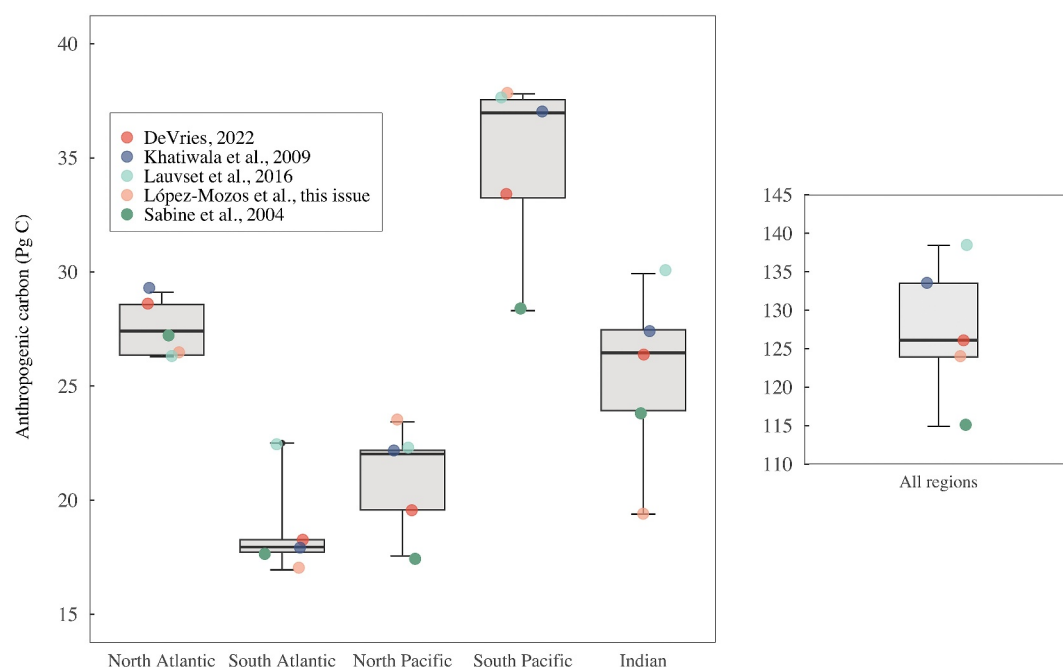


**Figure 4.** Boxplots of  $C_{\text{ant}}$  total inventories (Pg C), resulted from integration of  $C_{\text{ant}}$  column inventories over each ocean basin, normalized by each basin's product area and multiplied by a reference area (see Table S1 in Supporting Information S2). Individual data points represent results obtained from five independent methodologies of  $C_{\text{ant}}$  as specified in the figure legend: DeVries (2022; OCIMv2021, data-assimilation model), Khatiwala et al. (2009; Green function), Lauvset et al. (2016; TTD method), López-Mozos et al. (this issue; Back-Calculation) and Sabine et al. (2004; Back-Calculation). Each box plot corresponds to a specific ocean basin, with the last one (*All regions*) representing the sum of the first five. Negative values were removed for Sabine et al. (2004).

subtropical gyres of the Southern hemisphere. However, with respect to the other methodologies, and even among them, there are differences in the magnitude and location of that accumulation (Figure 3). In particular, our results agree with the TTD method and the OCIMv2021 model in the Argentine Basin, with a decreasing  $C_{\text{ant}}$  content toward the east. Interestingly, when looking to the total  $C_{\text{ant}}$  inventories, our results in the SA (16.9 Pg C) are slightly lower than other methodologies (Figure 4; Table S1 in Supporting Information S2), and are closer to Khatiwala et al. (2009) method (GF method hereafter) and the  $\Delta C^*$  method (Sabine et al., 2004). This suggests that, although our  $C_{\text{ant}}$  spatial pattern is consistent with other methodologies (Figure 3), our SA total  $C_{\text{ant}}$  inventory may be slightly underestimated (Figure 4). This potential underestimation is reasonable given that the SA region shows low dispersion among methods, and our results are quite close to the mean (Table S1 in Supporting Information S2). The lower value could be attributed to our relatively low  $C_{\text{ant}}$  values south of  $60^{\circ}\text{S}$  (Figure 3) which are included in the total SA inventory computation. South of  $60^{\circ}\text{S}$ , our  $C_{\text{ant}}$  depth-integrated values exhibit a significant reduction, making the Antarctic region one of the areas with our lowest  $C_{\text{ant}}$  column inventories (Figure 3). In the Antarctic region, our approach yields slightly higher values compared to the  $\Delta C^*$  method, with both methods reporting the lowest values. Further discussion will be addressed at Section 3.4.

In the Pacific basin, a contrast in  $C_{\text{ant}}$  column inventories becomes noticeable when comparing the southern and northern regions. The South Pacific (SP) region presents higher  $C_{\text{ant}}$  concentrations in comparison to its northern counterpart (Figure 3, panel A). Moreover, the SP has a higher total  $C_{\text{ant}}$  inventory (37.8 Pg C vs. 23.4 Pg C in the North Pacific), even when taking into account their respective areas (Table S1 in Supporting Information S2). This north-south difference is consistent with the rest of methodologies (Figure 3). Notably, this spatial distribution is characterized by a zonal gradient wherein  $C_{\text{ant}}$  concentrations gradually diminish from east to west in the southern region. In contrast, the northern region exhibits higher  $C_{\text{ant}}$  values closer to its western margin and the Sea of Okhotsk. The North Pacific (NP)  $C_{\text{ant}}$  column inventory (Figure 3, panel A) presents a similar pattern to the TTD method and OCIMv2021 model ones (Figure 3), but with a higher inventory (Figure 4). Interestingly, TrOCA method has been shown to overestimate  $C_{\text{ant}}$  globally and regionally (Table S1 in Supporting Information S2), but for the NP there is almost no detectable  $C_{\text{ant}}$  signal. The difference between our results and that of

TrOCA, despite using a common MCS data, reveals a feasible methodological divergence. We showed that the denitrification process has a low impact on the remineralization term compared to respiration (see Section 3.1.1). However, when integrated over depth can have a bigger impact on remineralization, especially in regions with high denitrification as the NP (Figure 2, panel K), supporting the relevance of accounting for denitrification in back-calculation approaches (e.g., Gruber & Sarmiento, 1997).

In the SP, we agree with the rest of methodologies by presenting a more horizontal-extensive  $C_{\text{ant}}$  column inventory (Figure 3). We present a maximum of  $C_{\text{ant}}$  in the subtropical region, coinciding with that of the TTD method, in a cyclonic structure, as already evidenced (e.g., Sabine et al., 2002). This maximum is more intense than that of the other methodologies, showing a wider structure than, for example, the TTD method, which is narrower. The similarity between our wider structure and the one presented by TrOCA and even the  $\Delta C^*$ , which presents a less intense accumulation, could be attributed to the MCS data of the region. On the other hand, the Indian Ocean has the same cyclonic structure of  $C_{\text{ant}}$  over the 30°S, which also appears in the methods that do not use MCS data, pointing such accumulation as quite realistic. In the Southern Indian, there is a similar pattern between our approach and OCIMv2021 model, and we also present similarities with the TTD and GF methods. In contrast, for the northern Indian, all methodologies present low values with a two-by-two agreement between OCIMv2021 and the GF method, the  $\Delta C^*$  and TTD methods, and TrOCA and our results. In the Indian Ocean, we show the regional total  $C_{\text{ant}}$  inventory farthest from the average of the methodologies used, almost 5 Pg C below it.

The total ocean  $C_{\text{ant}}$  inventory given by our approach is  $124 \pm 7$  Pg C, close to the median value among the other methods (Figure 4 and Table S1 in Supporting Information S2). Despite this, we present disparities at regional level compensated on a global scale (Figure 4 and Table S1 in Supporting Information S2). As already mentioned, our approach provides consistent values for the Atlantic Ocean (Figure 4), both at Northern and Southern basins, with slightly below-mean values for both regions. In contrast, in the Pacific Ocean we present slightly higher values when compared to the rest of methodologies, with the highest data dispersion among methods found in the South Pacific. Finally, in the Indian Ocean we provide the lowest values when compared to the rest. The next sections (Sections 3.3 and 3.4) will combine the outcomes of the sensitivity analysis and the deep- $C_{\text{ant}}$  column inventories. The results integration will contribute to discern if the differences can be attributed to the MCS data used and/or the proposed approach.

### 3.3. Sensitivity Analysis

Three sensitivity cases were considered (Section 2.5) to discern between the uncertainty generated by data-related errors (*Case I*) and methodological errors (*Case II*), as well as to quantify the final uncertainty of our method and the global  $C_{\text{ant}}$  inventory uncertainty (*Case III*). Data-related errors (Figure S8 in Supporting Information S1) contribute to the total method uncertainty by  $\pm 4.5 \mu\text{mol kg}^{-1}$ , which, when integrated over depth, actually generates a low uncertainty in the total inventory of  $C_{\text{ant}}$  (STD = 0.3 Pg C;  $N = 300$ ). This is consistent with the fact that random errors in measurements do not have a strong influence on total inventories, as long as they are not spatially biased (Müller et al., 2023) and compensate each other. In contrast, methodological errors (Figure S9 in Supporting Information S1) have a smaller impact on the total method uncertainty, of about  $\pm 0.1$  and  $2.2 \mu\text{mol kg}^{-1}$  for *subtype 1* and *subtype 2* respectively but, when integrated over depth, their contribution to the total inventory of  $C_{\text{ant}}$  uncertainty is larger than that of data-related errors (STD = 2.0 Pg C for *subtype 1*; STD = 6.7 Pg C for *subtype 2*; both  $N = 300$ ). The combination of the last two cases, that is, *Case III* (Figure S10 in Supporting Information S1), results in a total method uncertainty of  $\pm 5.6 \mu\text{mol kg}^{-1}$ , which is mainly governed by data-related errors along the water column (*Case I*); and a total  $C_{\text{ant}}$  inventory uncertainty of  $\pm 7.1$  Pg C, primarily governed by methodological errors (*Case II*)—more specifically, by the effect of errors on the TMI surface boundary conditions.

### 3.4. $C_{\text{ant}}$ Distribution at Depth

The total ocean  $C_{\text{ant}}$  inventory at depth (from 3,500 to 5,500 m) estimated by our approach is  $4.4 \pm 3.4$  Pg C. This amount, when multiplied by the mean annual  $C_{\text{ant}}$  growth rate from Gruber et al. (2019) of 1.9%, yields to an annual rate of  $0.08 \text{ Pg C yr}^{-1}$ . Over the 13 years of Gruber et al. (2019) study, this rate accounts for 1.2 Pg C at depth, which is consistent with Gruber et al. (2019) estimate of 1 Pg C at depth. The averaged  $C_{\text{ant}}$  below 3,500 m (Figure 5) also assesses and validates  $C_{\text{ant}}$  estimations by discerning whether the  $C_{\text{ant}}$  presence could be attributed to methodological uncertainty or a feasible presence of  $C_{\text{ant}}$  (Figure S11 in Supporting Information S1). Globally,

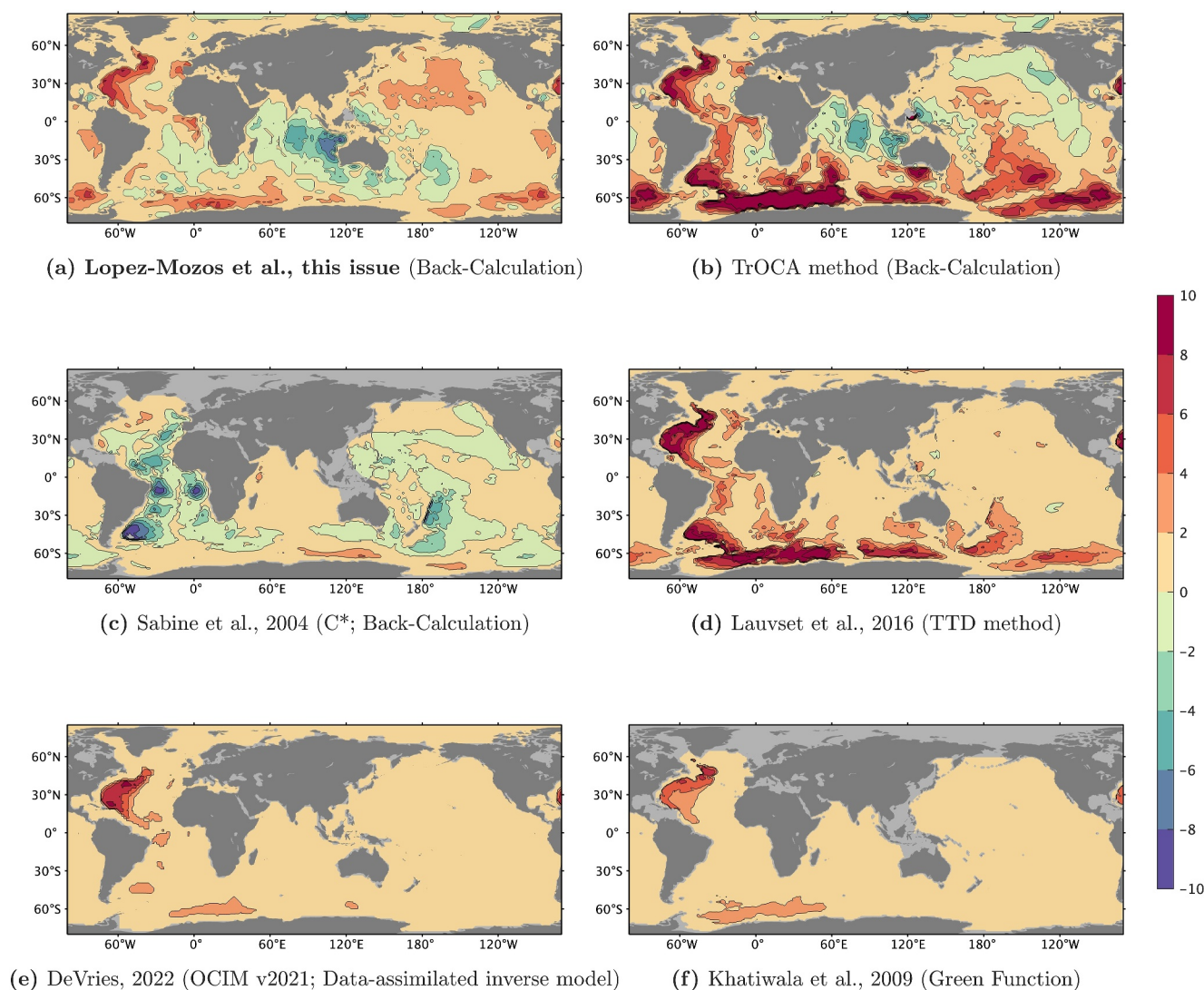


**Figure 5.** Averaged  $C_{\text{ant}}$  column concentration ( $\mu\text{molC kg}^{-1}$ ) integrated below 3 500 m up to 5,500 m (5,580 m for OCIM v2021), centered in 1995, from six independent  $C_{\text{ant}}$  methodologies. For Sabine et al. (2004) negative  $C_{\text{ant}}$  values have been maintained.

the spatial pattern of our deep- $C_{\text{ant}}$  results falls between the TTD method versus OCIMv2021 model GF method. In contrast, we mainly differ at depth with the  $\Delta C^*$ , with which, although we also show negative values in the global integral, the biases are not as negative and neither coincide spatially.

The elevated  $C_{\text{ant}}$  presence in the deep western NA coincides with the results of other methodologies and is also consistent with previous evidences of deep- $C_{\text{ant}}$  invasion in the NA (Gruber et al., 2019; Pérez et al., 2008; Raimondi et al., 2021; Rhein et al., 2017; Vázquez-Rodríguez et al., 2009). This suggests that a deep- $C_{\text{ant}}$  signal in the western NA is realistic, supported by the sensitivity analysis results (Figure S11 in Supporting Information S1). Moreover, we observe local  $C_{\text{ant}}$  signals along the Atlantic, such as in the deep Eastern NA basin or the Argentine Basin, which coincide with the TTD method and OCIMv2021, and are also consistent with previous studies (Ríos et al., 2010, 2012). The deep- $C_{\text{ant}}$  pattern in the SO, which matches the TTD method, suggests a realistic accumulation, as supported by the GF method and OCIMv2021 model which also show such invasion, especially between  $10^{\circ}\text{W}$ – $60^{\circ}\text{E}$  longitudes that comprises the Lazarev to Cooperation seas (Figure S11 in Supporting Information S1). This agrees with recent  $C_{\text{ant}}$  findings in the dominant water mass at depth (i.e., the AABW) in the SO for one decade later (Ohashi et al., 2023). In addition, it seems reasonable that our approach shows less accumulation of  $C_{\text{ant}}$  in the SO than the TTD method because of its full CFCs equilibrium assumption (Matear et al., 2003; Waugh et al., 2006). The SO is a region where the uncertainties of climate change are high

(Hauck et al., 2023), but there is increasing evidence, such as deep-warming (Kouketsu et al., 2011), suggesting that there could be more anthropogenic signal than expected from an ice-sheet isolated ocean. Additionally, in the Pacific-SO region we also present a deep- $C_{\text{ant}}$  signal, coinciding with both the TTD method and TrOCA patterns.

Similar to the  $C_{\text{ant}}$  integration above 3,500 m, the Indian and North Pacific regions exhibit distinct deep  $C_{\text{ant}}$ -accumulation patterns compared to the rest (Figure 5). In both regions, our method cannot demonstrate that  $C_{\text{ant}}$  presence is distinguishable from zero (Figure S11 in Supporting Information S1), indicating that the  $C_{\text{ant}}$  presence is not statistically significant. The North Pacific shows a slight mean positive  $C_{\text{ant}}$  concentration ( $1.7 \mu\text{mol kg}^{-1} \pm 1.0$ ; Figure 5) when compared to the methodologies that are not based on MCS data. In contrast, we observe a negative pattern in the Indian Ocean which aligns with the negative TrOCA pattern, a method used as an input-data consistency exercise. The match in negative bias suggests there may be an issue with the MCS data used. Furthermore, sensitivity test *Case II* revealed that the Indian Ocean has greater uncertainty at depth than other regions when altering imposed TMI surface boundary conditions. Additionally, bottom points around Australia and from Mawson to Ross Sea are subject to increased uncertainty (Gebbie & Huybers, 2010). Therefore, our biased results in the Indian Ocean could result from a combination of input-data quality and the methodological approach.

Interestingly, a recent study (Müller et al., 2023) showed that some cruises used for the GLODAPv2 database in the Indian Ocean provided their  $\text{CO}_2$  data slightly biased during the period used in this study, generating underestimations of  $C_{\text{ant}}$  in the Indian Ocean. This means that such bias could also affect the neural network (NN)-derived  $C_T$  and  $A_T$  climatological data we used here, which, once integrated over depth, could generate an impact because of the large volume of deep layers (Müller et al., 2023). Particularly, the study proposed corrections for the next update GLODAPv3 for the Indian Ocean that would explain - as they fit with - our negative-biased  $C_{\text{ant}}$  results in the region. Since our MCS data comes from a NN-derived climatology, we consider that such correction must be included in a new NN-MCS derived climatology with the next GLODAPv3 data, supporting the need for the program's continuity and its data quality control.

#### 4. Summary and Conclusions

We presented a back-calculation method to estimate the steady-state component of oceanic anthropogenic  $\text{CO}_2$  ( $C_{\text{ant}}$ ), that relies on marine carbonate-system (MCS) data-based climatologies and the steady-state ocean circulation model TMI (Gebbie & Huybers, 2010). This novel approach provides a coherent total  $C_{\text{ant}}$  inventory that compares well with other (four) independent methodologies, proving it to be a valid tool for back-calculation approaches, and supporting the versatility of data-assimilated inverse models for biogeochemistry studies (as in e.g., Carter et al., 2021; Davila et al., 2022; Lauvset et al., 2020; Liang et al., 2023; Sulpis et al., 2023).

As a novelty to former back-calculation methods, our method refined the oxygen saturation assumption by accounting for the sea-air oxygen disequilibrium, which enhances the global  $C_{\text{ant}}$  inventory estimate by 6%. However, and as inherent to all back-calculation approaches, the method is not exempt from limitations. The sensitivity analysis performed led us to conclude that the deep (below 3,500 m) inventories in the Indian and Pacific Oceans were the least confident estimates at the regional scale. Tracking-back potential sources of error, we related such regional discrepancies to limitations inherent to the input data and the TMI performance. Small surface areas in the TMI surface boundary conditions can have a large impact on the deep-ocean (Gebbie & Huybers, 2011). As such, if the quality of the data in these boundary-condition regions is compromised due to, for example, scarce sampling coverage, then the propagation of its less accurately determined surface properties to depth might influence the deep regional  $C_{\text{ant}}$  inventories. Besides, since most of the total  $C_{\text{ant}}$  inventory uncertainty also comes from the errors at the surface TMI boundary conditions, it would also influence the magnitude of the final uncertainty. In this study, the MCS data climatology used was centered in 1995, and based on in-situ data spanning 1972–2012. Thus, our result is subject to the propagation of surface boundary conditions in certain under sampled regions, as in the Southern Ocean, which might have impacted the regional deep  $C_{\text{ant}}$  inventory estimates of the Indian and Pacific Oceans. The advancement in new climatologies based on the most recent observations (e.g., WOA23, Keppler et al., 2023; Kolodziejczyk et al., 2024) will open up the possibility of extending MCS based- $C_{\text{ant}}$  inventories beyond the 2000s, and thus likely reducing the input-data limitation of the present method.

Another important point to consider is the surface boundary condition for the  $\Delta C_{\text{dis}}^{\pi}$  term. Getting this term is not trivial, and future work should be addressed to explore alternative ways to compute it, for instance, by means of

numerical simulations (Matsumoto & Gruber, 2005) and/or a compendium of the most recent Coupled Model Intercomparison Project (CMIP6) models. Finally, recent advances are also opening the door to include the seasonal variability of the ocean circulation transport operators in inverse modeling (Huang et al., 2021), so the approach presented here could be applied to other mixing schemes.

Assessing the distribution and storage of  $C_{\text{ant}}$  in the ocean is crucial in the context of climate change (Inter-governmental Panel on Climate Change IPCC, 2019). Nevertheless, it implies distinguishing a signal of less than 4% from the dissolved inorganic carbon ocean reservoir, for which no single optimal method exists. Hence, we need to continue advancing with a broad range of approaches. In situ MCS data are the most accurate ocean carbon data sets to date. Sustained international research programs like GO-SHIP, along with the Global Ocean Data Analysis Project (GLODAP) quality control efforts, are essential for providing the research community with full-depth global ocean highly accurate MCS data, which serve as a key reference data set for, for example, model validation, artificial intelligence (AI) learning and verification, or novel autonomous sensor calibration. This study emphasizes the value of MCS data-based approaches to compute  $C_{\text{ant}}$  inventories by providing a useful proof-of-concept method that will serve as a base for further progress.

### Conflict of Interest

The authors declare no conflicts of interest relevant to this study.

### Data Availability Statement

The Total Matrix Intercomparison software (TMI) can be accessed at Gebbie et al. (2023). The climatologies of  $A_T$ ,  $C_T$ , oxygen and nutrients are available at the data repository of the Spanish National Research Council (CSIC); <https://digital.csic.es/handle/10261/194411> Broullón et al., 2019; <http://hdl.handle.net/10261/200537>; Broullón et al., 2020). Khatiwala et al. (2009)'s product used can be accessed at Müller (2023).

### Acknowledgments

The authors thank the editor-in-chief Stephen Griffies, and are grateful for the formal review and constructive comments from an anonymous associate editor and two anonymous reviewers. M. López-Mozos was supported by the grant PRE2020-093138 funded by MICIU/AEI/10.13039/501100011033 and by "ESF Investing in your future". F. F. Pérez was supported by the FICARAM+ project (PID2023-148924OB-I00). A. Velo was supported by the BOCATS2 (PID2019-104279GB-C21) project funded by MICIU/AEI/10.13039/501100011033, and by EuroGO-SHIP project (Horizon Europe #101094690). L.I. Carracedo was supported by Ifremer. This work is also a contribution to OCEANS + CSIC PTI efforts.

### References

- Álvarez, M., Pérez, F. F., Bryden, H., & Ríos, A. F. (2004). Physical and biogeochemical transports structure in the North Atlantic subpolar gyre. *Journal of Geophysical Research*, 109(C3), C03027. <https://doi.org/10.1029/2003JC002015>
- Anderson, L. A. (1995). On the hydrogen and oxygen content of marine phytoplankton. *Deep Sea Research Part I: Oceanographic Research Papers*, 42(9), 1675–1680. [https://doi.org/10.1016/0967-0637\(95\)00072-E](https://doi.org/10.1016/0967-0637(95)00072-E)
- Anderson, L. A., & Sarmiento, J. L. (1994). Redfield ratios of remineralization determined by nutrient data analysis. *Global Biogeochemical Cycles*, 8(1), 65–80. <https://doi.org/10.1029/93GB03318>
- Bednaršek, N., Feely, R. A., Pelletier, G., & Desmet, F. (2023). Global synthesis of the status and trends of ocean acidification impacts on shelled pteropods. *Oceanography*, 36(2/3), 130–137. <https://doi.org/10.5670/oceanog.2023.210>
- Bittig, H. C., Steinhoff, T., Claustre, H., Fiedler, B., Williams, N. L., Sauzède, R., et al. (2018). An alternative to static climatologies: Robust estimation of open Ocean CO<sub>2</sub> variables and nutrient concentrations from T, S, and O<sub>2</sub> data using Bayesian neural networks. *Frontiers in Marine Science*, 5, 340855. <https://doi.org/10.3389/fmars.2018.00328>
- Bockmon, E. E., & Dickson, A. G. (2015). An inter-laboratory comparison assessing the quality of seawater carbon dioxide measurements. *Marine Chemistry*, 171, 36–43. <https://doi.org/10.1016/j.marchem.2015.02.002>
- Brewer, P. G. (1978). Direct observation of the oceanic CO<sub>2</sub> increase. *Geophysical Research Letters*, 5(12), 997–1000. <https://doi.org/10.1029/GL005i012p00997>
- Broecker, W., Takahashi, T., Simpson, H., & Peng, T.-H. (1979). Fate of fossil fuel carbon dioxide and the global carbon budget. *Science*, 206(4417), 409–418. <https://doi.org/10.1126/science.206.4417.409>
- Broecker, W. S. (1974). "NO", a conservative water-mass tracer. *Earth and Planetary Science Letters*, 23(1), 100–107. [https://doi.org/10.1016/0012-821X\(74\)90036-3](https://doi.org/10.1016/0012-821X(74)90036-3)
- Broecker, W. S., & Peng, T.-H. (1982). *Tracers in the Sea*. Lamont-Doherty Geological Observatory, Columbia University.
- Broullón, D., Pérez, F. F., Velo, A., Hoppema, M., Olsen, A., Takahashi, T., et al. (2019). A global monthly climatology of total alkalinity: A neural network approach. *Earth System Science Data*, 11(3), 1109–1127. <https://doi.org/10.5194/essd-11-1109-2019>
- Broullón, D., Pérez, F. F., Velo, A., Hoppema, M., Olsen, A., Takahashi, T., et al. (2020). A global monthly climatology of oceanic total dissolved inorganic carbon: A neural network approach. *Earth System Science Data*, 12(3), 1725–1743. <https://doi.org/10.5194/essd-12-1725-2020>
- Carter, B. R., Feely, R. A., Lauvset, S. K., Olsen, A., DeVries, T., & Sonnerup, R. (2021). Preformed properties for marine organic matter and carbonate mineral cycling quantification. *Global Biogeochemical Cycles*, 35(1), e2020GB006623. <https://doi.org/10.1029/2020GB006623>
- Carter, B. R., Toggweiler, J. R., Key, R. M., & Sarmiento, J. L. (2014). Processes determining the marine alkalinity and calcium carbonate saturation state distributions. *Biogeosciences*, 11(24), 7349–7362. <https://doi.org/10.5194/bg-11-7349-2014>
- Chen, G.-T., & Millero, F. J. (1979). Gradual increase of oceanic CO<sub>2</sub>. *Nature*, 277(5693), 205–206. <https://doi.org/10.1038/277205a0>
- Cianca, A., Helmke, P., Mouriño, B., Rueda, M. J., Llina's, O., & Neuer, S. (2007). Decadal analysis of hydrography and in situ nutrient budgets in the western and eastern North Atlantic subtropical gyre. *Journal of Geophysical Research*, 112(C7), C07025. <https://doi.org/10.1029/2006JC003788>
- Craig, H. (1971). The deep metabolism: Oxygen consumption in abyssal ocean water. *Journal of Geophysical Research* (1896-1977), 76(21), 5078–5086. <https://doi.org/10.1029/JC076i021p05078>
- Davila, X., Gebbie, G., Brakstad, A., Lauvset, S. K., McDonagh, E. L., Schwinger, J., & Olsen, A. (2022). How is the ocean anthropogenic carbon reservoir filled? *Global Biogeochemical Cycles*, 36(5), e2021GB007055. <https://doi.org/10.1029/2021GB007055>



- DeVries, T. (2022). Atmospheric CO<sub>2</sub> and sea surface temperature variability cannot explain recent decadal variability of the Ocean CO<sub>2</sub> sink. *Geophysical Research Letters*, *49*(7), e2021GL096018. <https://doi.org/10.1029/2021GL096018>
- DeVries, T., Yamamoto, K., Wanninkhof, R., Gruber, N., Hauck, J., Müller, J. D., et al. (2023). Magnitude, trends, and variability of the Global Ocean carbon sink from 1985 to 2018. *Global Biogeochemical Cycles*, *37*(10), e2023GB007780. <https://doi.org/10.1029/2023GB007780>
- Dickson, A. G. (1990). Standard potential of the reaction: AgCl (s) + 1/2H<sub>2</sub> (g) = Ag (s) + HCl (aq), and, and the standard acidity constant of the ion HSO<sub>4</sub><sup>-</sup> in synthetic seawater from 273.15 to 318.15 K. *The Journal of Chemical Thermodynamics*, *22*(2), 113–127. [https://doi.org/10.1016/0021-9614\(90\)90074-Z](https://doi.org/10.1016/0021-9614(90)90074-Z)
- Dickson, A. G., Afghan, J. D., & Anderson, G. C. (2003). Reference materials for oceanic CO<sub>2</sub> analysis: A method for the certification of total alkalinity. *Marine Chemistry*, *80*(2), 185–197. [https://doi.org/10.1016/S0304-4203\(02\)00133-0](https://doi.org/10.1016/S0304-4203(02)00133-0)
- Duteil, O., Koeve, W., Oschlies, A., Bianchi, D., Galbraith, E., Kriest, I., & Matear, R. (2013). A novel estimate of ocean oxygen utilisation points to a reduced rate of respiration in the ocean interior. *Biogeosciences*, *10*(11), 7723–7738. <https://doi.org/10.5194/bg-10-7723-2013>
- Feely, R. A., Jiang, L.-Q., Wanninkhof, R., Carter, B. R., Alin, S. R., Bednaršek, N., & Cosca, C. E. (2023). Acidification of the global surface ocean: What we have learned from observations. *Oceanography*, *36*(2/3), 120–129. <https://doi.org/10.5670/oceanog.2023.222>
- Feely, R. A., Sabine, C. L., Lee, K., Berelson, W., Kleypas, J., Fabry, V. J., & Millero, F. J. (2004). Impact of anthropogenic CO<sub>2</sub> on the CaCO<sub>3</sub> system in the oceans. *Science*, *305*(5682), 362–366. <https://doi.org/10.1126/science.1097329>
- Fraga, F., Ríos, A. F., Pérez, F. F., & Figueiras, F. G. (1998). Theoretical limits of oxygen:carbon and oxygen:nitrogen ratios during photosynthesis and mineralisation of organic matter in the sea. *Scientia Marina*, *62*(1–2), 161–168. <https://doi.org/10.3989/scimar.1998.62n1-2161>
- Francois, R., Honjo, S., Krishfield, R., & Manganini, S. (2002). Factors controlling the flux of organic carbon to the bathypelagic zone of the ocean. *Global Biogeochemical Cycles*, *16*(4), 34–34–20. <https://doi.org/10.1029/2001GB001722>
- Friedlingstein, P., O'Sullivan, M., Jones, M. W., Andrew, R. M., Bakker, D. C. E., Hauck, J., et al. (2023). Global carbon budget 2023. *Earth System Science Data*, *15*(12), 5301–5369. <https://doi.org/10.5194/essd-15-5301-2023>
- Fröb, F., Olsen, A., Pérez, F. F., García-Ibáñez, M. I., Jeansson, E., Omar, A., & Lauvset, S. K. (2018). Inorganic carbon and water masses in the Irminger Sea since 1991. *Biogeosciences*, *15*(1), 51–72. <https://doi.org/10.5194/bg-15-51-2018>
- Fu, W., Moore, J. K., Primeau, F., Collier, N., Ogunro, O. O., Hoffman, F. M., & Randerson, J. T. (2022). Evaluation of ocean biogeochemistry and carbon cycling in CMIP Earth system models with the international ocean model benchmarking (IOMB) software system. *Journal of Geophysical Research: Oceans*, *127*(10), e2022JC018965. <https://doi.org/10.1029/2022JC018965>
- Gebbie, G., Hamilton, B. R., & Davila, X. (2023). TMLjl: Total Matrix Intercomparison software tools for global ocean circulation (v0.2.0) [Software]. *Zenodo*. <https://doi.org/10.5281/zenodo.8226802>
- Gebbie, G., & Huybers, P. (2010). Total matrix Intercomparison: A method for determining the geometry of water-mass pathways. *Journal of Physical Oceanography*, *40*(8), 1710–1728. <https://doi.org/10.1175/2010JPO4272.1>
- Gebbie, G., & Huybers, P. (2011). How is the ocean filled? *Geophysical Research Letters*, *38*(6). <https://doi.org/10.1029/2011GL046769>
- Gebbie, G., & Huybers, P. (2012). The mean age of ocean waters inferred from radiocarbon observations: Sensitivity to surface sources and accounting for mixing histories. *Journal of Physical Oceanography*, *42*(2), 291–305. <https://doi.org/10.1175/JPO-D-11-043.1>
- Gruber, N., Clement, D., Carter, B. R., Feely, R. A., van Heuven, S., Hoppema, M., et al. (2019). The oceanic sink for anthropogenic CO<sub>2</sub> from 1994 to 2007. *Science*, *363*(6432), 1193–1199. <https://doi.org/10.1126/science.aau5153>
- Gruber, N., & Sarmiento, J. L. (1997). Global patterns of marine nitrogen fixation and denitrification. *Global Biogeochemical Cycles*, *11*(2), 235–266. <https://doi.org/10.1029/97GB00077>
- Gruber, N., Sarmiento, J. L., & Stocker, T. F. (1996). An improved method for detecting anthropogenic CO<sub>2</sub> in the oceans. *Global Biogeochemical Cycles*, *10*(4), 809–837. <https://doi.org/10.1029/96GB01608>
- Hall, T. M., Haine, T. W. N., & Waugh, D. W. (2002). Inferring the concentration of anthropogenic carbon in the ocean from tracers. *Global Biogeochemical Cycles*, *16*(4), 1131. <https://doi.org/10.1029/2001GB001835>
- Hansell, D. A. (2013). Recalcitrant dissolved organic carbon fractions. *Annual Review of Marine Science*, *5*(1), 421–445. <https://doi.org/10.1146/annurev-marine-120710-100757>
- Hansell, D. A., & Carlson, C. A. (2014). *Biogeochemistry of marine dissolved organic matter*. Academic Press.
- Hauck, J., Gregor, L., Nissen, C., Patara, L., Hague, M., Mongwe, P., et al. (2023). The Southern Ocean carbon cycle 1985–2018: Mean, seasonal cycle, trends, and storage. *Global Biogeochemical Cycles*, *37*(11), e2023GB007848. <https://doi.org/10.1029/2023GB007848>
- Hauck, J., & Völker, C. (2015). Rising atmospheric CO<sub>2</sub> leads to large impact of biology on Southern Ocean CO<sub>2</sub> uptake via changes of the Revelle factor. *Geophysical Research Letters*, *42*(5), 1459–1464. <https://doi.org/10.1002/2015GL063070>
- Huang, Q., Primeau, F., & DeVries, T. (2021). Cyclocim: A 4-D variational assimilation system for the climatological mean seasonal cycle of the ocean circulation. *Ocean Modelling*, *159*, 101762. <https://doi.org/10.1016/j.ocemod.2021.101762>
- IGBP, IOC and SCOR. (2013). *Ocean acidification summary for policymakers – third symposium on the Ocean in a high-CO<sub>2</sub> World*. International Geosphere-Biosphere Programme.
- Intergovernmental Panel on Climate Change, IPCC. (2019). Technical summary. H.-O. Pörtner, D. C. Roberts, V. Masson-Delmotte, P. Zhai, M. Tignor, et al. (eds.). In: *IPCC Special Report on the Ocean and Cryosphere in a Changing Climate*. (pp. 39–69). Cambridge University Press. <https://doi.org/10.1017/9781009157964.002>
- Iselin, C. O. D. (1939). The influence of vertical and lateral turbulence on the characteristics of the waters at mid-depths. *Eos. Transactions - American Geophysical Union*, *20*(3), 414–417. <https://doi.org/10.1029/TR020i003p00414>
- Ito, T. J., Follows, M. J., & Boyle, E. A. (2004). Is AOU a good measure of respiration in the oceans? *Geophysical Research Letters*, *31*(17), L17305. <https://doi.org/10.1029/2004GL020900>
- Jeansson, E., Tanhua, T., Olsen, A., Smethie, W. M., Rajasakaren, B., Ólafsdóttir, S. R., & Ólafsson, J. (2023). Decadal changes in ventilation and anthropogenic carbon in the Nordic seas. *Journal of Geophysical Research: Oceans*, *128*(3), e2022JC019318. <https://doi.org/10.1029/2022JC019318>
- Johnson, K. S., Plant, J. N., Dunne, J. P., Talley, L. D., & Sarmiento, J. L. (2017). Annual nitrate drawdown observed by SOCCOM profiling floats and the relationship to annual net community production. *Journal of Geophysical Research: Oceans*, *122*(8), 6668–6683. <https://doi.org/10.1002/2017JC012839>
- Keppler, L., Landschützer, P., Lauvset, S. K., & Gruber, N. (2023). Recent trends and variability in the oceanic storage of dissolved inorganic carbon. *Global Biogeochemical Cycles*, *37*(5), e2022GB007677. <https://doi.org/10.1029/2022GB007677>
- Khatiwal, S., Primeau, F., & Hall, T. (2009). Reconstruction of the history of anthropogenic CO<sub>2</sub> concentrations in the ocean. *Nature*, *462*(7271), 346–349. <https://doi.org/10.1038/nature08526>
- Khatiwal, S., Schmittner, A., & Muglia, J. (2019). Air-sea disequilibrium enhances ocean carbon storage during glacial periods. *Science Advances*, *5*(6), eaaw4981. <https://doi.org/10.1126/sciadv.aaw4981>

- Khatiwal, S., Tanhua, T., Mikaloff Fletcher, S., Gerber, M., Doney, S. C., Graven, H. D., et al. (2013). Global ocean storage of anthropogenic carbon. *Biogeosciences*, *10*(4), 2169–2191. <https://doi.org/10.5194/bg-10-2169-2013>
- Klaas, C., & Archer, D. E. (2002). Association of sinking organic matter with various types of mineral ballast in the deep sea: Implications for the rain ratio. *Global Biogeochemical Cycles*, *16*(4), 63–1–63–14. <https://doi.org/10.1029/2001GB001765>
- Koeve, W., & Kähler, P. (2016). Oxygen utilization rate (our) underestimates ocean respiration: A model study. *Global Biogeochemical Cycles*, *30*(8), 1166–1182. <https://doi.org/10.1002/2015GB005354>
- Kolodziejczyk, N., Portela, E., Thierry, V., & Prigent, A. (2024). ISASO2: Recent trends and regional patterns of Ocean Dissolved Oxygen change [Preprint]. *Earth System Science Data Discussions*, *16*(11), 5191–5206. <https://doi.org/10.5194/essd-2024-106>
- Körtzinger, A., Hedges, J. I., & Quay, P. D. (2001). Redfield ratios revisited: Removing the biasing effect of anthropogenic CO<sub>2</sub>. *Limnology & Oceanography*, *46*(4), 964–970. <https://doi.org/10.4319/lo.2001.46.4.0964>
- Körtzinger, A., Rhein, M., & Mintrop, L. (1999). Anthropogenic CO<sub>2</sub> and CFCs in the North Atlantic Ocean—A comparison of man-made tracers. *Geophysical Research Letters*, *26*(14), 2065–2068. <https://doi.org/10.1029/1999GL900432>
- Kouketsu, S., Doi, T., Kawano, T., Masuda, S., Sugiura, N., Sasaki, Y., et al. (2011). Deep ocean heat content changes estimated from observation and reanalysis product and their influence on sea level change. *Journal of Geophysical Research*, *116*(C3), C03012. <https://doi.org/10.1029/2010JC006464>
- Lauvset, S. K., Carter, B. R., Pérez, F. F., Jiang, L.-Q., Feely, R. A., Velo, A., & Olsen, A. (2020). Processes driving global interior ocean pH distribution. *Global Biogeochemical Cycles*, *34*(1), e2019GB006229. <https://doi.org/10.1029/2019GB006229>
- Lauvset, S. K., Key, R. M., Olsen, A., van Heuven, S., Velo, A., Lin, X., et al. (2016). A new global interior ocean mapped climatology: The 1°x1° GLODAP version 2. *Earth System Science Data*, *8*(2), 325–340. <https://doi.org/10.5194/essd-8-325-2016>
- Lewis, E., & Wallace, D. W. R. (1998). Program developed for CO<sub>2</sub> system calculations. ORNL/CDIAC-105, Carbon Dioxide Information Analysis Center, Oak Ridge National Laboratory, US Department of Energy. <https://doi.org/10.2172/639712>
- Liang, H., Lunstrum, A. M., Dong, S., Berelson, W. M., & John, S. G. (2023). Constraining CaCO<sub>3</sub> export and dissolution with an ocean alkalinity inverse model. *Global Biogeochemical Cycles*, *37*(2), e2022GB007535. <https://doi.org/10.1029/2022GB007535>
- Liu, M., & Tanhua, T. (2021). Water masses in the Atlantic Ocean: Characteristics and distributions. *Ocean Science*, *17*(2), 463–486. <https://doi.org/10.5194/os-17-463-2021>
- Locarnini, R. A., Mishonov, A. V., Antonov, J. I., Boyer, T. P., Garcia, H. E., Baranova, O. K., et al. (2013). In S. Levitus & A. Mishonov Technical. *World Ocean Atlas 2013, volume 1: Temperature*. (Eds.) (Vol. 73, p. 40). NOAA Atlas NESDIS.
- Lo Monaco, C., Metz, N., Poisson, A., Brunet, C., & Schauer, B. (2005). Anthropogenic CO<sub>2</sub> in the Southern Ocean: Distribution and inventory at the Indian-Atlantic boundary (World Ocean circulation experiment line I6). *Journal of Geophysical Research*, *110*(C6), C06010. <https://doi.org/10.1029/2004JC002643>
- Matear, R. J., Wong, C. S., & Xie, L. (2003). Can CFCs be used to determine anthropogenic CO<sub>2</sub>? *Global Biogeochemical Cycles*, *17*(1). <https://doi.org/10.1029/2001GB001415>
- Matsumoto, K., & Gruber, N. (2005). How accurate is the estimation of anthropogenic carbon in the ocean? An evaluation of the ΔC\* method. *Global Biogeochemical Cycles*, *19*(3), GB3014. <https://doi.org/10.1029/2004GB002397>
- McDougall, T. J., & Barker, P. M. (2011). Getting started with TEOS-10 and the Gibbs Seawater (GSW) oceanographic toolbox. *SCOR/IAPSO WG, 127*(532), 1–28.
- Middelburg, J. J. (2019). Marine carbon biogeochemistry: A primer for Earth system scientists. *Springer Nature*. <https://doi.org/10.1007/978-3-030-10822-9>
- Müller, J. D. (2023). RECCAP2-ocean data collection [Dataset]. <https://doi.org/10.5281/zenodo.7990823>
- Müller, J. D., Gruber, N., Carter, B., Feely, R., Ishii, M., Lange, N., et al. (2023). Decadal trends in the oceanic storage of anthropogenic carbon from 1994 to 2014. *AGU Advances*, *4*(4), e2023AV000875. <https://doi.org/10.1029/2023AV000875>
- Ohashi, Y., Yamamoto-Kawai, M., Kusahara, K., Sasaki, K., & Ohshima, K. I. (2023). Circumpolar distributions of age and anthropogenic CO<sub>2</sub> content of Antarctic Bottom Water revealed by chlorofluorocarbon and sulfur hexafluoride. *Progress in Oceanography*, *219*, 103153. <https://doi.org/10.1016/j.poccean.2023.103153>
- Pardo, P. C., Pérez, F. F., Khatiwal, S., & Ríos, A. F. (2014). Anthropogenic CO<sub>2</sub> estimates in the Southern Ocean: Storage partitioning in the different water masses. *Progress in Oceanography*, *120*, 230–242. <https://doi.org/10.1016/j.poccean.2013.09.005>
- Pardo, P. C., Vázquez-Rodríguez, M., Pérez, F. F., & Ríos, A. F. (2011). CO<sub>2</sub> air–sea disequilibrium and preformed alkalinity in the Pacific and Indian oceans calculated from subsurface layer data. *Journal of Marine Systems*, *84*(3–4), 67–77. <https://doi.org/10.1016/j.jmarsys.2010.08.006>
- Pérez, F. F., & Fraga, F. (1987). The pH measurements in seawater on the NBS scale. *Marine Chemistry*, *21*(4), 315–327. [https://doi.org/10.1016/0304-4203\(87\)90054-5](https://doi.org/10.1016/0304-4203(87)90054-5)
- Pérez, F. F., Vázquez-Rodríguez, M., Louarn, E., Padín, X. A., Mercier, H., & Ríos, A. F. (2008). Temporal variability of the anthropogenic CO<sub>2</sub> storage in the Irminger Sea. *Biogeosciences*, *5*(6), 1669–1679. <https://doi.org/10.5194/bg-5-1669-2008>
- Pérez, F. F., Vázquez-Rodríguez, M., Mercier, H., Velo, A., Lherminier, P., & Ríos, A. F. (2010). Trends of anthropogenic CO<sub>2</sub> storage in North Atlantic water masses. *Biogeosciences*, *7*(5), 1789–1807. <https://doi.org/10.5194/bg-7-1789-2010>
- Qiu, B., & Huang, R. X. (1995). Ventilation of the North Atlantic and North Pacific: Subduction versus obduction. *Journal of Physical Oceanography*, *25*(10), 2374–2390. [https://doi.org/10.1175/1520-0485\(1995\)025<2374:VOTNAA>2.0.CO;2](https://doi.org/10.1175/1520-0485(1995)025<2374:VOTNAA>2.0.CO;2)
- Raimondi, L., Tanhua, T., Azetsu-Scott, K., Yashayaev, I., & Wallace, D. W. R. (2021). A 30-year time series of transient tracer-based estimates of anthropogenic carbon in the Central Labrador Sea. *Journal of Geophysical Research: Oceans*, *126*(5), e2020JC017092. <https://doi.org/10.1029/2020JC017092>
- Redfield, A. C., Ketchum, B. H., & Richards, F. A. (1963). The influence of organisms on the composition of seawater. *The sea*, *2*, 26–77.
- Reid, J. L. (1997). On the total geostrophic circulation of the Pacific Ocean: Flow patterns, tracers and transports. *Progress in Oceanography*, *39*(4), 263–352. [https://doi.org/10.1016/S0079-6611\(97\)00012-8](https://doi.org/10.1016/S0079-6611(97)00012-8)
- Rhein, M., Steinfeldt, R., Kieke, D., Stendardo, I., & Yashayaev, I. (2017). Ventilation variability of Labrador Sea water and its impact on oxygen and anthropogenic carbon: A review. *Philosophical Transactions of the Royal Society A: Mathematical, Physical & Engineering Sciences*, *375*(2102), 20160321. <https://doi.org/10.1098/rsta.2016.0321>
- Ríos, A. F., Vázquez-Rodríguez, M., Padín, X. A., & Pérez, F. F. (2010). Anthropogenic carbon dioxide in the South Atlantic western basin. *Journal of Marine Systems*, *83*(1), 38–44. <https://doi.org/10.1016/j.jmarsys.2010.06.010>
- Ríos, A. F., Velo, A., Pardo, P. C., Hoppema, M., & Pérez, F. F. (2012). An update of anthropogenic CO<sub>2</sub> storage rates in the western South Atlantic basin and the role of Antarctic Bottom Water. *Journal of Marine Systems*, *94*(0), 197–203. <https://doi.org/10.1016/j.jmarsys.2011.11.023>

- Rubin, S. I., & Key, R. M. (2002). Separating natural and bomb-produced radiocarbon in the ocean: The potential alkalinity method. *Global Biogeochemical Cycles*, 16(4), 52–1–52–19. <https://doi.org/10.1029/2001GB001432>
- Sabine, C. L., Feely, R. A., Gruber, N., Key, R. M., Lee, K., Bullister, J. L., et al. (2004). The oceanic sink for anthropogenic CO<sub>2</sub>. *Science*, 305(5682), 367–371. <https://doi.org/10.1126/science.1097403>
- Sabine, C. L., Feely, R. A., Key, R. M., Bullister, J. L., Millero, F. J., Lee, K., et al. (2002). Distribution of anthropogenic CO<sub>2</sub> in the Pacific Ocean. *Global Biogeochemical Cycles*, 16(4). <https://doi.org/10.1029/2001GB001639>
- Sabine, C. L., Key, R. M., Johnson, K. M., Millero, F. J., Poisson, A., Sarmiento, J. L., et al. (1999). Anthropogenic CO<sub>2</sub> inventory of the Indian ocean. *Global Biogeochemical Cycles*, 13(1), 179–198. <https://doi.org/10.1029/1998GB900022>
- Sharp, J. D., Pierrot, D., Humphreys, M. P., Epitalon, J.-M., Orr, J. C., Lewis, E. R., & Wallace, D. W. R. (2021). CO<sub>2</sub>SYsv3 for MATLAB [Computer software]. *Zenodo*. <https://doi.org/10.5281/zenodo.4774718>
- Stommel, H. (1979). Determination of water mass properties of water pumped down from the Ekman layer to the geostrophic flow below. *Proceedings of the National Academy of Sciences*, 76(7), 3051–3055. <https://doi.org/10.1073/pnas.76.7.3051>
- Sulpis, O., Lauvset, S. K., & Hagens, M. (2020). Current estimates of K<sub>1</sub>\* and K<sub>2</sub>\* appear inconsistent with measured CO<sub>2</sub> system parameters in cold oceanic regions. *Ocean Science*, 16(4), 847–862. <https://doi.org/10.5194/os-16-847-2020>
- Sulpis, O., Trossman, D. S., Holzer, M., Jeansson, E., Lauvset, S. K., & Middelburg, J. J. (2023). Respiration patterns in the dark ocean. *Global Biogeochemical Cycles*, 37(8), e2023GB007747. <https://doi.org/10.1029/2023GB007747>
- Talley, L. (2013). Closure of the global overturning circulation through the Indian, Pacific, and southern oceans: Schematics and transports. *Oceanography*, 26(1), 80–97. <https://doi.org/10.5670/oceanog.2013.07>
- Tomczak, M., & Large, D. G. (1989). Optimum multiparameter analysis of mixing in the thermocline of the eastern Indian Ocean. *Journal of Geophysical Research*, 94(C11), 16141–16149. <https://doi.org/10.1029/JC094iC11p16141>
- Touratier, F., Azouzi, L., & Goyet, C. (2007). CFC-11, Δ14C and 3H tracers as a means to assess anthropogenic CO<sub>2</sub> concentrations in the ocean. *Tellus B: Chemical and Physical Meteorology*, 59(2), 318–325. <https://doi.org/10.1111/j.1600-0889.2006.00247.x>
- Touratier, F., & Goyet, C. (2004a). Applying the new TrOCA approach to assess the distribution of anthropogenic CO<sub>2</sub> in the Atlantic Ocean. *Journal of Marine Systems*, 46(1), 181–197. <https://doi.org/10.1016/j.jmarsys.2003.11.020>
- Touratier, F., & Goyet, C. (2004b). Definition, properties, and Atlantic Ocean distribution of the new tracer TrOCA. *Journal of Marine Systems*, 46(1), 169–179. <https://doi.org/10.1016/j.jmarsys.2003.11.016>
- Troupin, C., Barth, A., Sirjacobs, D., Ouberdous, M., Brankart, J.-M., Brasseur, P., et al. (2012). Generation of analysis and consistent error fields using the Data Interpolating Variational Analysis (DIVA). *Ocean Modelling*, 52–53, 90–101. <https://doi.org/10.1016/j.ocemod.2012.05.002>
- Uppström, L. R. (1974). The boron/chlorinity ratio of deep-sea water from the Pacific Ocean. *Deep-Sea Research and Oceanographic Abstracts*, 21(2), 161–162. [https://doi.org/10.1016/0011-7471\(74\)90074-6](https://doi.org/10.1016/0011-7471(74)90074-6)
- van Heuven, S., Pierrot, D., Rae, J. W. B., Lewis, E., & Wallace, D. W. R. (2011). *MATLAB program developed for CO<sub>2</sub> system calculations*. ORNL/CDIAC-105b. Carbon Dioxide Information Analysis Center, Oak Ridge National Laboratory, U.S. Department of Energy. [https://doi.org/10.3334/CDIAC/otg.CO2SYS\\_MATLAB\\_v1.1](https://doi.org/10.3334/CDIAC/otg.CO2SYS_MATLAB_v1.1)
- Vázquez-Rodríguez, M., Padín, X. A., Pardo, P. C., Ríos, A. F., & Pérez, F. F. (2012). The subsurface layer reference to calculate preformed alkalinity and air–sea CO<sub>2</sub> disequilibrium in the Atlantic Ocean. *Journal of Marine Systems*, 94, 52–63. <https://doi.org/10.1016/j.jmarsys.2011.10.008>
- Vázquez-Rodríguez, M., Touratier, F., Lo Monaco, C., Waugh, D. W., Padín, X. A., Bellerby, R. G. J., et al. (2009). Anthropogenic carbon distributions in the Atlantic Ocean: Data-based estimates from the Arctic to the Antarctic. *Biogeosciences*, 6(3), 439–451. <https://bg.copernicus.org/articles/6/439/2009/>
- Völker, C., Wallace, D. W. R., & Wolf-Gladrow, D. A. (2002). On the role of heat fluxes in the uptake of anthropogenic carbon in the North Atlantic. *Global Biogeochemical Cycles*, 16(4), 85–1–85–9. <https://doi.org/10.1029/2002GB001897>
- Wanninkhof, R., Doney, S. C., Peng, T. H., Bullister, J. L., Lee, K., & Feely, R. A. (1999). Comparison of methods to determine the anthropogenic CO<sub>2</sub> invasion into the Atlantic Ocean. *Tellus B: Chemical and Physical Meteorology*, 51(2), 511–530. <https://doi.org/10.3402/tellusb.v51i2.16335>
- Waugh, D. W., Hall, T. M., McNeil, B. I., Key, R., & Matear, R. J. (2006). Anthropogenic CO<sub>2</sub> in the oceans estimated using transit time distributions. *Tellus B: Chemical and Physical Meteorology*, 58(5), 376–389. <https://doi.org/10.1111/j.1600-0889.2006.00222.x>
- Williams, R. G., Marshall, J. C., & Spall, M. A. (1995). Does Stommel's mixed layer “demon” work? *Journal of Physical Oceanography*, 25(12), 3089–3102. [https://doi.org/10.1175/1520-0485\(1995\)025<3089:DSMLW>2.0.CO;2](https://doi.org/10.1175/1520-0485(1995)025<3089:DSMLW>2.0.CO;2)
- Yool, A., Oschlies, A., Nurser, A. J. G., & Gruber, N. (2010). A model-based assessment of the TrOCA approach for estimating anthropogenic carbon in the ocean. *Biogeosciences*, 7(2), 723–751. <https://doi.org/10.5194/bg-7-723-2010>
- Zeebe, R., & Wolf-Gladrow, D. (2001). *CO<sub>2</sub> in Seawater: Equilibrium, kinetics, isotopes*, Elsevier oceanography. Ser. (Vol. 65, p. 346). Elsevier.
- Zweng, M. M., Reagan, J. R., Antonov, J. I., Locarnini, R. A., Mishonov, A. V., Boyer, T. P., et al. (2013). In S. Levitus & A. Mishonov Technical. *World Ocean Atlas 2013, volume 2: Salinity*. (Eds.) (39, Vol. 74). NOAA Atlas NESDIS.